Global and Planetary Change 68 (2009) 100–114

Contents lists available at ScienceDirect

Global and Planetary Change

journal homepage: www.elsevier.com/locate/gloplacha

Impact of diagenesis on the environmental magnetic record from a Holocene sedimentary sequence from the Chukchi–Alaskan margin, Arctic Ocean

Stefanie Brachfeld [a,*], Francesco Barletta [b], Guillaume St-Onge [b], Dennis Darby [c], Joseph D. Ortiz [d]

[a] Department of Earth and Environmental Studies, Montclair State University, Montclair, NJ 07043, USA
[b] Institut des sciences de la mer de Rimouski (ISMER) and GEOTOP Research Center, 310 allée des Ursulines, Rimouski, QC, Canada G5L 3A1
[c] Department of Ocean, Earth, and Atmospheric Sciences, Old Dominion, University, Norfolk, VA 23529, USA
[d] Department of Geology, Kent State Univ., Kent, OH 44242, USA

ARTICLE INFO

Article history:
Accepted 31 March 2009
Available online 24 April 2009

Keywords:
environmental magnetism
Chukchi Sea
greigite
diagenesis

ABSTRACT

We present a high-resolution Holocene sedimentary record of environmental variability from the eastern Chukchi Sea. An ice-rafted debris bearing silty-clay marks the deglacial to post-glacial Holocene transition at this site and is dated at 9.7 ka. An interval of oscillating magnetic parameters from 9.5 to 8.7 ka coincides with the Holocene Thermal Maximum in the western Arctic, and is manifested at the study area as pulses of fine-grained magnetite input every 180–230 years, possibly from increased river discharge or stronger currents flowing over the core site. The magnetic mineral assemblage is very uniform over the last 8.2 ka and consists of a mixture of magnetite, titanomagnetite, and a magnetic phase that we tentatively identify as the magnetic iron sulfide greigite. The amount of magnetic iron sulfides increases up through the Holocene, a trend that is controlled by the amount of marine organic matter available to fuel bacterial sulfate reduction. The median destructive field of the Natural Remanent Magnetization (MDF_{NRM}) displays centennial to millennial scale cycles with significant variance at periods of 900–1300 and 1700–2700 years, with intervals of high MDF_{NRM} values coinciding with indicators of greater sea ice cover [McKay, J., de Vernal, A., Hillaire-Marcel, C., Not, C., Polyak, L., Darby, D., 2008. Holocene fluctuations in Arctic sea-ice cover: Dinocyst-based reconstructions for the eastern Chukchi Sea. Can. J. Earth Sci. 45, 1399–1415]. The MDF_{NRM} is controlled by the variable abundance of iron sulfides formed during early diagenesis. We interpret intervals of high MDF_{NRM} values as times of stronger water column stratification, during which the pyritization process was interrupted by the lack of marine organic matter and lack of reactive iron. Intervals of low MDF_{NRM} values, which coincide with indicators of reduced sea ice cover, are interpreted as times of stronger vertical mixing of the water column, which allows fresh marine organic matter and reactive iron to reach the seafloor, driving the pyritization process to completion.

© 2009 Published by Elsevier B.V.

1. Introduction

Leg 1 of the 2005 Healy-Oden Trans-Arctic Expedition (HOTRAX-05) conducted a marine geological and geophysical study of the eastern Chukchi Sea (Darby et al., 2005). A combination of swath bathymetry mapping, 3.5-kHz CHIRP subsurface profiling, and jumbo piston coring was used to target thick Holocene sediment accumulations that would allow investigation into the nature and timing of deglaciation in the western Arctic Ocean, determination of the past extent of sea ice cover in the western Arctic Ocean, the history of surface ocean circulation in the Arctic, and the Holocene variability of the geomagnetic field at high northern latitudes. A suite of jumbo piston cores was collected along the edge of the continental shelf and upper continental slope North of Barrow, Alaska, (Fig. 1) at sites positioned to record changes in the Beaufort Gyre, the Transpolar Drift, and the inflow of Pacific water through the Bering Strait (Darby et al., 2005; Darby et al., 2009-this volume; Ortiz et al., 2009-this volume; Polyak et al., 2009-this volume).

The Holocene units in cores HLY05-01 JPC5, JPC6 and JPC8 (Fig. 1) have been analyzed for the construction of geomagnetic paleosecular variation (PSV) and relative paleointensity (RPI) records, which are presented in Barletta et al., 2008, and Lisé-Pronovost et al. (2009-this volume). These are among the first high-resolution Holocene geomagnetic records from the Arctic Ocean that are constrained by a radiocarbon chronology. This study focuses on the environmental magnetic record from JPC5, a 16.48-m long jumbo piston core that contains an expanded Holocene section and penetrates into pre-Holocene glacial-marine sediment. Magnetic mineral assemblages can serve as tracers of sediment provenance, and by inference, sediment transport processes such as ice rafting, fluvial input, eolian transport, bottom current intensity, and biological productivity (e.g., Robinson, 1986; Kissel et al., 1997, 1999; Stoner and Andrews, 1999; Brachfeld

* Corresponding author. Tel.: +1 973 655 5129; fax: +1 973 655 4072.
E-mail address: brachfelds@mail.montclair.edu (S. Brachfeld).

0921-8181/$ – see front matter © 2009 Published by Elsevier B.V.
doi:10.1016/j.gloplacha.2009.03.023

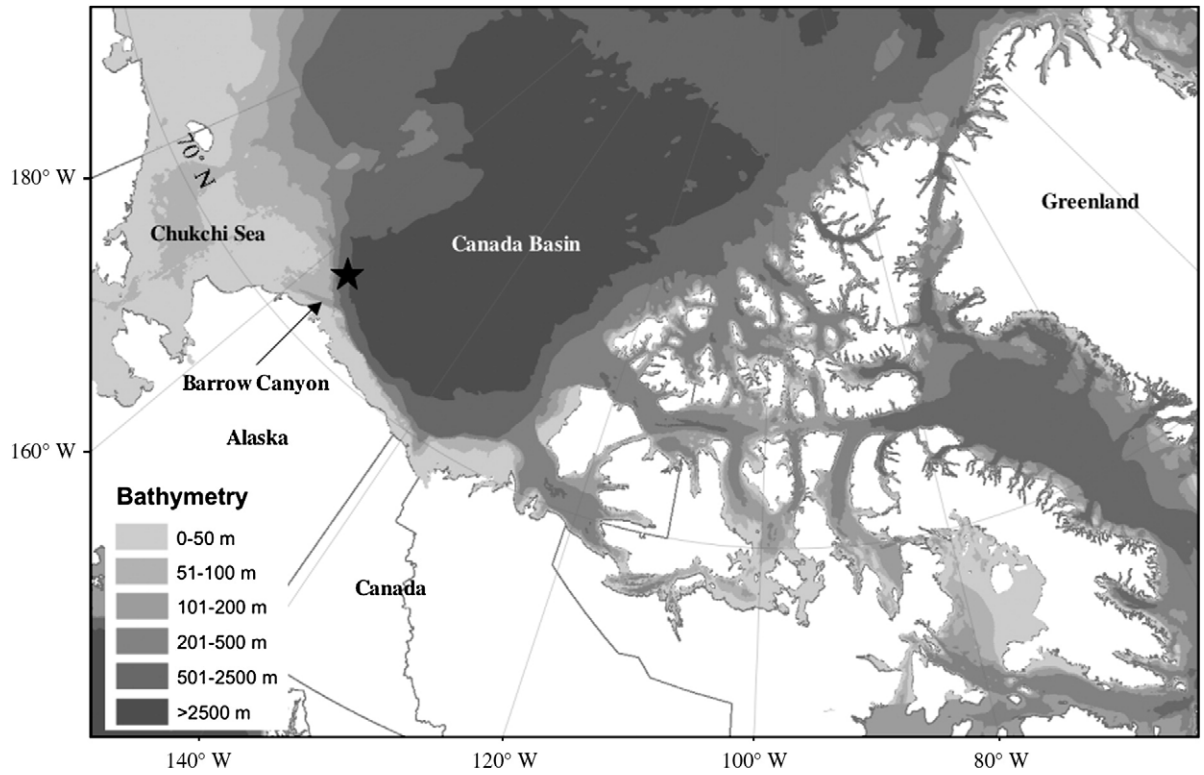

Fig. 1. Location map showing the position of core HLY05-01 JPC5 (black star) on the upper continental slope just offshore of northwest Alaska. Bathymetry data are from Jakobsson et al. (2008a).

et al., 2002; Kissel et al., 2003; Muhs et al., 2003; Hounslow and Morton, 2004; Brachfeld, 2006; Reynolds et al., 2006; Rousse et al., 2006; Blanchet et al., 2007). Magnetic parameters may be particularly useful in the Arctic Ocean, where the abundance of foraminifers and diatoms are low, and their preservation potential uneven to poor in the sedimentary record. Magnetic parameters are sensitive indicators of post-depositional diagenesis that impact both paleomagnetic signals and paleoclimatic signals (e.g., Karlin and Levi, 1983; Leslie et al., 1990), but which can also track environmental conditions that affect the geochemistry of the water column and the sediment column (e.g., Snowball and Torii, 1999; Sagnotti et al., 2001; Larrasoaña et al., 2003, 2007).

JPC5 contains a continuous 9700-year expanded Holocene section that is constrained by Accelerator Mass Spectrometer (AMS) radiocarbon dates. The magnetic mineral record is remarkably uniform with the exception of one parameter, MDF_{NRM}, which displays centennial to millennial scale oscillations. Here we examine the interplay of detrital and authigenic magnetic minerals and their impacts on the MDF_{NRM}.

2. Study area

HLY05-01 JPC5 and its trigger core TC5 were collected from the eastern Chukchi Sea, North of Barrow, Alaska (72.694° N, 157.520° W, 415 m water depth) during cruise 05–01 of the *USCGC Healy*. The core site is on the upper continental slope in a region where numerous small canyons dissect the continental slope and flow into the Canada Basin. JPC5 was collected on the western flank of one of these small canyons. 3.5-kHz CHIRP sub-bottom profiles were used to select core sites. Core JPC5 was collected from an acoustically semitransparent seismic unit that drapes the underlying bedrock. This post-glacial unit reaches thicknesses of nearly 20-m, and contains faint parallel laminations (Polyak et al., 2007; Jakobsson et al., 2008a,b). Thick sediment accumulations in this area likely result from a combination of riverine input that is redistributed by currents, and melt out of sediment from sea ice (Darby et al., 2009-this volume; Ortiz et al., 2009-this volume). JPC5 penetrated into the high-amplitude reflector at the base of the semitransparent unit, recovering 13 m of silty clay and nearly 4 m of the underlying sandy mud and diamicton.

The water column structure at the core site and other nearby sites was measured during cruise HLY05-01 using a Seabird CTD (Fig. 2). The upper 0–45 m is characterized by a cold, low-salinity surface layer, whose temperature and salinity are influenced by river runoff and sea ice melting during the summer. The Pacific layer is present from 45 to 150 m, and is composed of water that flows into the Arctic Ocean through the shallow Bering Strait. Below 150-m is the relatively warm and high-salinity Atlantic layer that enters the Arctic Ocean through the Fram Strait (Aagaard et al., 1981; Weingartner et al., 1998; Codispoti et al., 2005; Woodgate et al., 2005; Serreze et al., 2006). Dissolved oxygen at the core site decreases from a high of 7.35 mL/L at the surface to 5 mL/L near the sea floor.

3. Methods

Bottom sampling during cruise HLY05-01 was conducted using a 4 in.-diameter jumbo piston corer and trigger weight core. A multicorer with a rosette of 8 core tubes was used to collect an undisturbed sample of the sediment-water interface. Water column profiles were collected during cruise HLY05-01 using a Seabird CTD (SBE 9). Data were processed using SBE Data Processing Version 5.37e Win 32. The salinity data are presented on the PSS-90 scale.

Jumbo piston cores and trigger cores were split, photographed, and described, then sampled with u-channels for paleomagnetic analyses and Computerized Axial Tomography (CAT)-scans (Barletta et al., 2008; Lisé-Pronovost et al., 2009-this volume), with the exception of JPC5 section 1, which was too watery to collect a u-channel. However, the uppermost sediment column was recovered intact in the trigger core at Station 5 (TC5). U-channels were measured for the stepwise

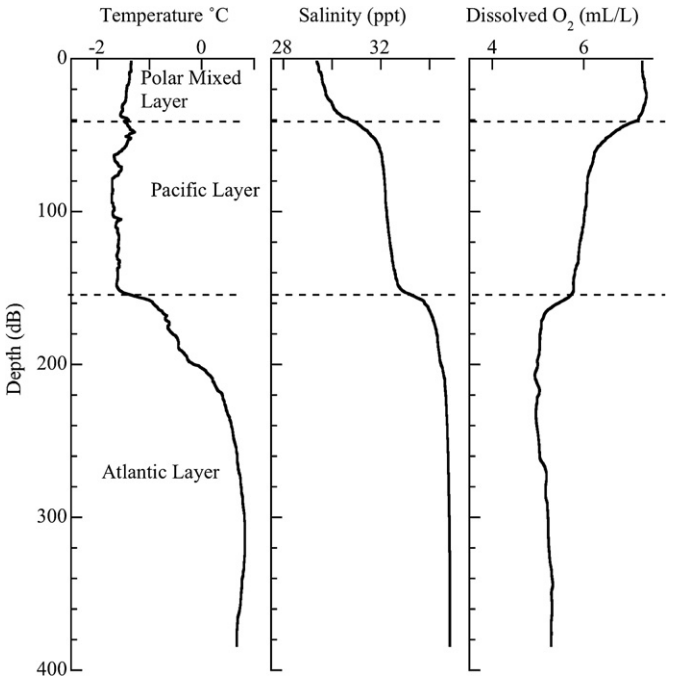

Fig. 2. Present-day hydrography at HLY05-01 station 5. The water column is strongly stratified, with the cold fresh Polar Mixed Layer (PML) from 0 to 45 m, the Pacific Layer from 40 to 150 m, and the warm, saline Atlantic Layer below 150 m.

alternating field (AF) demagnetization of the Natural Remanent Magnetization (NRM), the stepwise acquisition and demagnetization of Anhysteretic Remanent Magnetization (ARM), and stepwise acquisition and demagnetization of the Isothermal Remanent Magnetization (IRM). Measurements were made on a 2G-Enterprises Model 760R u-channel magnetometer at the University of Florida, Gainesville, FL. The details of the demagnetization levels and the instrument parameters used to analyze TC5 and JPC5 are described elsewhere (Barletta et al., 2008; Lisé-Pronovost et al., 2009-this volume). Alternating field demagnetization data were used to calculate the median destructive field of the NRM (MDF_{NRM}), which is the alternating field demagnetization level at which the intensity of the NRM is reduced by 50% of its original value.

After the paleomagnetic measurements and CAT scans were completed, discrete sub-samples were removed from the u-channel every 5-cm. The sedimentation rate in JPC5 is approximately 145–160 cm/kyr. Therefore 5-cm corresponds to a ~30–35 year sampling interval. Sediments were freeze-dried and 200–300 mg of dry sediment was packed into gelatin capsules for measurements of magnetic susceptibility and hysteresis parameters. Low-field mass-normalized magnetic susceptibility (χ_{LF}) of dry samples was measured on an AGICO KLY-4 Kappabridge in an applied field of 300 A/m. The measurement of dry samples allows us to examine the behavior of the mineral content without the dilution effect of water. Ferromagnetic susceptibility (χ_F) was calculated by subtracting the high-field slope (χ_{HF}) of the magnetization (M) vs. applied field (H) curve measured on a vibrating sample magnetometer from χ_{LF}.

Magnetic hysteresis measurements were made on a Princeton Measurements Corp. micro-Vibrating Sample Magnetometer model 3900-04 at Montclair State University, NJ. Hysteresis loops were measured in a peak field of 1 T and field increments of 5 mT. Raw data were processed by using χ_{HF}, calculated from 0.7 to 1 T, to remove the paramagnetic contribution to the induced magnetization, and then normalized by dry mass. The hysteresis parameters saturation magnetization (M_S), saturation remanence (M_R) and coercivity (H_C) were determined from the paramagnetic-corrected data. The coercivity of remanence (H_{CR}) was determined through the DC-demagnetization of a saturation isothermal remanent magnetization imparted in a 1 T field. The S-ratio was measured by imparting a 1 T isothermal remanent magnetization, followed by the application of a 300 mT backfield, and calculating $M_{R(-300\ mT)}/M_{R(1\ T)}$. Stepwise acquisition of IRM was conducted on the VSM at 50 mT increments up to a maximum applied field of 1.75 T.

Magnetic susceptibility vs. temperature was measured on an AGICO KLY-4 Kappabridge equipped with a CS furnace using approximately 200–250 mg of dry sediment. Measurements were made from 40 to 700 °C in a flowing argon gas atmosphere. Measurements were made during heating to 700 °C and during cooling back down to room temperature to assess the degree of thermochemical alteration induced during the experiment. Raw data were normalized to dry mass of the sample. Low-temperature order/disorder transitions were observed using a Quantum Design Magnetic Properties Measurements System (MPMS) at the Institute for Rock Magnetism, University of Minnesota. We monitored the temperature dependence of saturation isothermal remanent magnetization ($M_R - T$) imparted in a 2.5 T field at 10 K and at 300 K.

Magnetic extracts were made using a two-step process. We used sodium polytungstate heavy liquid with specific gravity of 2.89 to separate heavy minerals. Several grams of dry bulk sediment was mixed with the heavy liquid, sonicated for 1 h to disaggregate the sample, and then centrifuged at 4700 revolutions per minute (rpm) for 30 min. After centrifuging the light fraction was decanted and the heavy fraction at the bottom of the centrifuge tube was washed with deionized water. We then separated magnetic grains from the heavy fraction using a rare-earth magnet. Magnetic extracts were imaged on a Hitachi S-3400N variable pressure scanning electron microscope (SEM) with a Bruker X-flash X-ray microanalysis system at Montclair State University.

4. Chronology

A combination of ^{210}Pb dating and Accelerator Mass Spectrometer (AMS) radiocarbon dating of calcareous shells was used to construct the depth-age model for TC5 and JPC5. A detailed discussion of the samples, species identification, selection of a reservoir correction, and conversion to calendar ages is presented in Darby et al. (2009-this volume), Barletta et al. (2008), and McKay et al. (2008). A brief summary is given here. Six bivalve shells were AMS radiocarbon dated at the Lawrence Livermore AMS facility and converted to calendar ages using Calib 5.0.2 (http://calib.qub.ac.uk/calib/calib.html). We used a ΔR value of zero, which represents a local reservoir age of 400 years (Stuiver and Reimer, 1993; Stuiver et al., 1998). We made a second calibration using a ΔR value of 460 years based on the radiocarbon ages of pre-1940s mollusks reported by McNeely et al., 2006. We include both sets of calibrated ages in Table 1 due to the uncertainty in the reservoir age for the study area. This paper uses the $\Delta R = 0$ dataset to derive a depth-age relationship for JPC5. This selection is based on a comparison of the geomagnetic inclination record in JPC5 (Barletta et al., 2008) to the paleomagnetic secular variation data for western

Table 1
Radiocarbon dates.

Core	Depth (mcd)	Uncorrected age (^{14}C yr BP)	Calibrated age (yr BP) ΔR = 0	Calibrated age (yr BP) ΔR = 460	Carbon source	Lab. number
JPC5	1.12	1930 ± 45	1477	1011	*Thyasira sp.*	CAMS-128414
JPC5	5.59	4465 ± 40	4656	4006	*Yolida sp.*	CAMS-128415
JPC5	6.64	4820 ± 70	5091	4510	*Thyasira sp.*	CAMS-128416
JPC5	7.64	5220 ± 40	5569	5007	*Yolida sp.*	CAMS-128417
JPC5	8.75	5885 ± 40	6303	5804	*Portlandia sp.*	CAMS-128418
JPC5	9.55	6395 ± 45	6867	6343	*Port.* + *Thya.*	CAMS-128419

North America (PSVL) derived from volcanic samples (Hagstrum and Champion, 2002), and with model output from the CALS7K.2 Holocene geomagnetic field model (Korte et al., 2005). The chronologies for PSVL and CALS7K.2 are both independent of the marine radiocarbon reservoir effect. The JPC5 inclination record dated with the $\Delta R = 0$ age model is very similar to PSVL and the CALS7K.2 profile generated for the study area coordinates, supporting the use of $\Delta R = 0$ (see Fig. 11a in Barletta et al., 2008).

A meter composite depth (mcd) scale was determined for TC5 and JPC5 by correlating downcore physical properties including GRAPE bulk density, natural gamma radiation (NGR), and spectral reflectance measurements (Barletta et al., 2008). The depth scale of JPC5 has been adjusted downwards by 75 cm based on these correlations. All subsequent core depths are reported as mcd. A linear regression was fit to the calendar age (calibrated using $\Delta R = 0$ years) vs. mcd to determine a depth-age relationship (Fig. 3). The data show a steady progression of ages with depth with no age reversals. The sedimentation rate is 145–150 cm/kyr in the upper 9.5 mcd. This is very similar to ^{210}Pb-derived sedimentation rate of 160.5 cm/kyr observed in TC5 (McKay et al., 2008), and comparable to the sedimentation rates reported for other Chukchi shelf and slope Holocene sediments (Keigwin et al., 2006). The linear depth-age trend was applied from 0 to 13.45 mcd, which contains Holocene silty-clay. The projected age at 13.45 mcd is approximately 9.7 ka. The age of the lithologic units below 13.45 mcd are unknown, but they likely represent the deglacial interval.

5. Results

5.1. Lithostratigraphy

JPC5 recovered two main lithologic units, which we further subdivide on the basis of magnetic parameters (see following section). Unit 1 (0–13.45 mcd) consists of homogeneous olive gray mud. From 0 to 13.15 mcd the sediment contains abundant shiny black speckles that occur in spots or diffuse laminae, which are likely iron sulfides (Figs. 4, 5). The abundance of visible black speckles and laminae gradually decreases below 10.80 mcd. From 13.15–13.45 mcd we observed white-colored carbonate clasts that are likely ice rafted debris (IRD).

Unit 2 encompasses 13.45 mcd to the base of the core (Fig. 5). This unit shows a variety of textures including laminated intervals, mud clots, and intervals of 'cottage cheese' texture. From 13.45 to 14.05 mcd the sediment consists of dark olive gray mud with scattered sand and ice rafted debris. From 14.05 to 14.71 mcd we observe olive gray mud alternating with grayish brown to olive brown and dark grayish brown sandy and clumpy mud layers. From 14.71 to 15.32 mcd the sediment is grayish brown to dark grayish brown mud that is finely laminated with scattered sand and mud clumps. The interval 15.32 to 16.01 mcd is characterized by very dark gray to grayish brown sandy clumpy mud with "cottage cheese" texture. The base of core (16.01–17.23 mcd) is composed of dark gray, moderately stiff homogeneous mud with scattered sand and ice rafted debris.

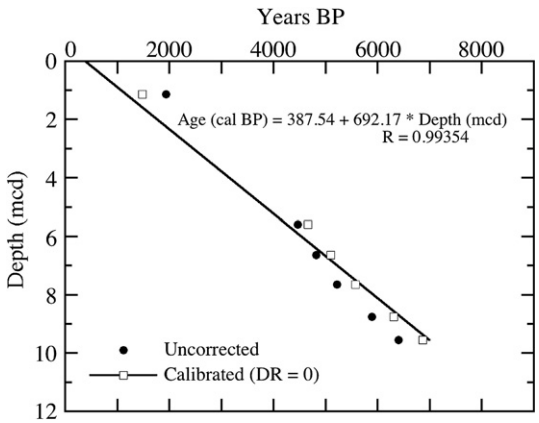

Fig. 3. Depth-age relationship derived from the $\Delta R = 0$ radiocarbon ages in Table 1. We assume that the top of TC5 is zero age, or −55 yr BP. A least-squares line fit to the calibrated ages has been applied to JPC5 from 0 to 13.45 mcd, yielding an age of approximately 9.7 ka at the base of the Holocene post-glacial unit.

5.2. Concentration-dependent magnetic parameters

Unit 1 is subdivided on the basis of magnetic parameters. Concentration-dependent parameters including χ_{LH}, M_S, ARM, and SIRM are highest in the trigger core and from 0 to 4.50 mcd in JPC5 (Unit 1a), and are relatively stable within this interval (Figs. 4, 5). There is a very slight step decrease in these parameters below 4.50 mcd, which then experience a slow steady decrease with depth in the core continuing down to 11.20 mcd (base of Unit 1b). Low field magnetic susceptibility values (χ_{LF}) range from 1 to $4*10^{-7}$ m^3/kg. High-field magnetic susceptibility (χ_{HF}) values, which track the paramagnetic and diamagnetic components of the sediment assemblage, range from 0.8 to $1*10^{-7}$ m^3/kg, reflecting the high proportion of paramagnetic material relative to ferrimagnetic material in the sediment. The χ_{HF} profile in Unit 1 contains both short- and long-wavelength variations, but increases slightly with depth.

An interval of low χ_{LH}, M_S, ARM, and SIRM occurs from 11.20 to 13.45 mcd (Unit 1c), which roughly coincides with the disappearance of the black speckles and laminae. SIRM shows high values in the lower half of Unit 1c from 12.80 to 13.45 mcd, coinciding with the appearance of white-colored IRD and the increasing abundance of sand. In Unit 2 there is no systematic relationship between the concentration-dependent magnetic parameters and sediment color or texture.

5.3. Magnetic "grain size" parameters

Parameters that are sensitive to magnetic domain-state, and hence grain volume, are stable in the trigger core and Unit 1a (Figs. 4, 6, 7). Samples from this interval plot in the pseudo-single-domain (PSD) field on a Day Plot (Fig. 7; Day et al., 1977). The ratio of saturation remanence normalized by saturation magnetization (M_R/M_S) range from 0.20 to 0.24 (Fig. 7). Similar stability occurs in H_C and H_{CR}. Hysteresis parameters do not exhibit the same subdivisions within Unit 1 that are seen in the concentration-dependent parameters. Hysteresis parameters are stable down to 12.00 mcd. However, the grain-size parameters ARM/SIRM and k_{ARM}/k do show the same subdivisions described above, with a step increase below 4.50 mcd, and decreasing values from 11.20 to 13.45 mcd.

From 12.00 to 13.45 mcd hysteresis parameters are characterized by large-amplitude swings (Fig. 6), which is indicative of either a change in magnetic particle size and/or a change in the magnetic mineralogy. ARM/SIRM and k_{ARM}/k values are low in this interval, with muted ARM/SIRM features coinciding with the M_R/M_S spikes. Samples from Unit 2 also fall within the PSD region of the Day Plot, but with M_R/M_S values generally <2, and a wider range of H_{CR}/H_C values than was observed in Unit 1. The MDF of the NRM (MDF_{NRM}) fluctuates between 10 and 55 mT within Unit 1 (Fig. 6). The MDF_{NRM} is significantly more variable than either the magnetic concentration indicators or the magnetic-domain state indicators, with decimeter- to meter-scale peaks and troughs.

5.4. Magnetic mineral composition

The upper 11.65 mcd of Unit 1a displays S-ratio values that are >0.94, consistent with, but not diagnostic of, minerals such as magnetite,

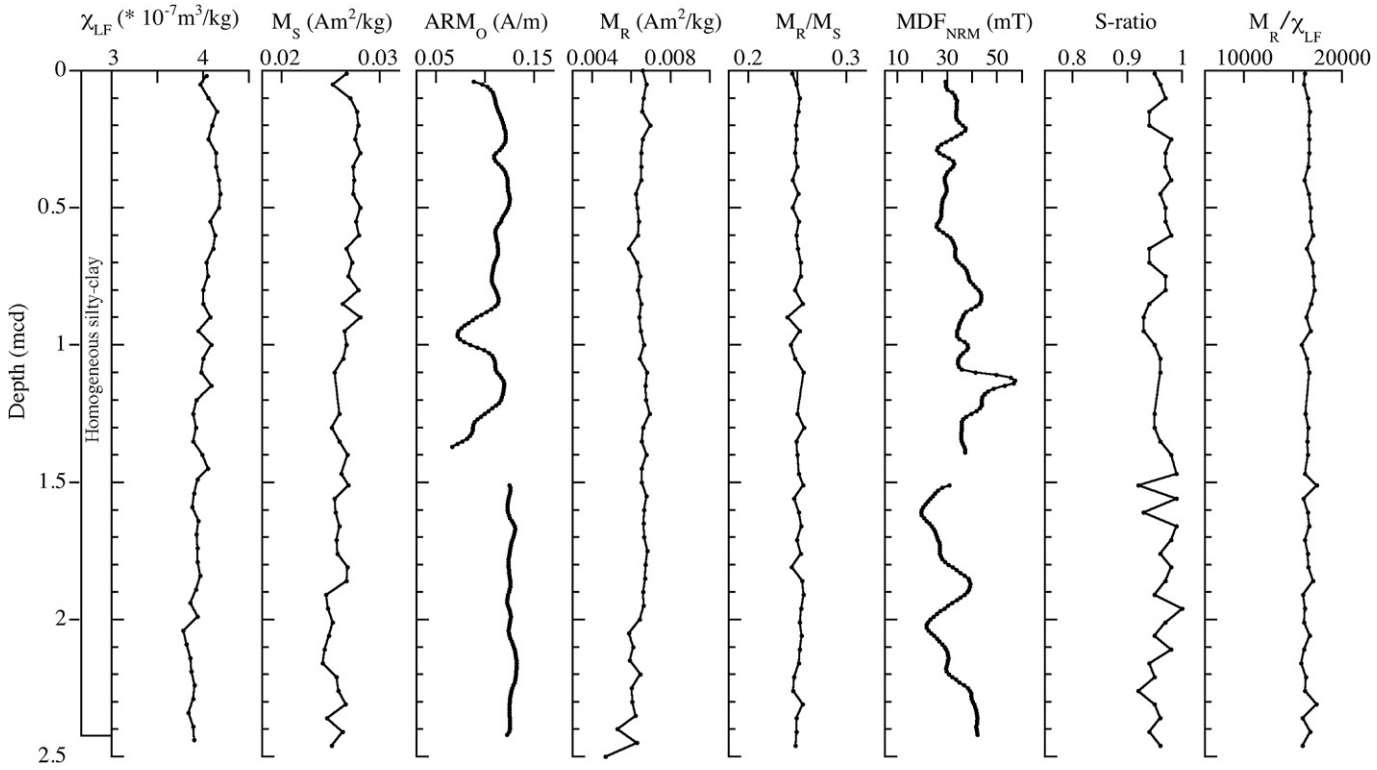

Fig. 4. Lithostratigraphy and rock magnetic parameters for Trigger Core 5 (TC5). From left to right: low-field mass-normalized magnetic susceptibility (χ_{LF}), saturation magnetization (M_S), anhysteretic remanent magnetization (ARM), saturation remanence (M_R), saturation remanence normalized by saturation magnetization (M_R/M_S), median destructive field of the natural remanent magnetization (MDF_{NRM}), S-ratio, and saturation remanence normalized by ferromagnetic susceptibility (M_R/χ_F). The lithostratigraphy and magnetic mineral assemblage in TC5 is very uniform. The exception is the MDF_{NRM}, which shows decimeter-scale highs and lows.

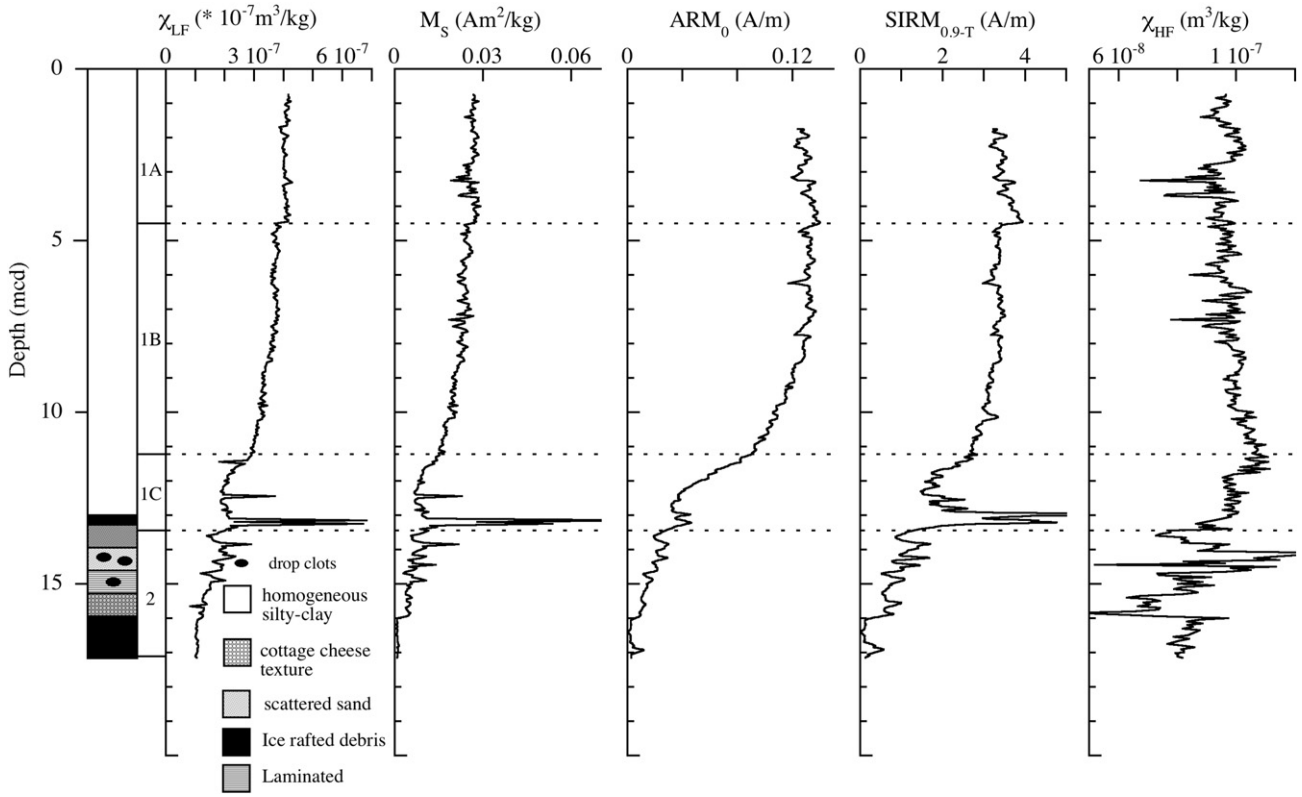

Fig. 5. Lithostratigraphy and concentration-dependent rock magnetic parameters vs. meters composite depth (mcd) for JPC5. From left to right: χ_{LF}, M_S, ARM, saturation isothermal remanent magnetization (SIRM), and high-field magnetic susceptibility (χ_{HF}). The core is divided into a pre-Holocene unit (Unit 2) and the overlying Holocene silty-clay (Unit 1). The concentration of magnetic material is uniform in the upper 11.15 mcd, and then gradually decreases with depth within Unit 1c. Peaks in these parameters at the base of Unit 1c coincide with an IRD layer.

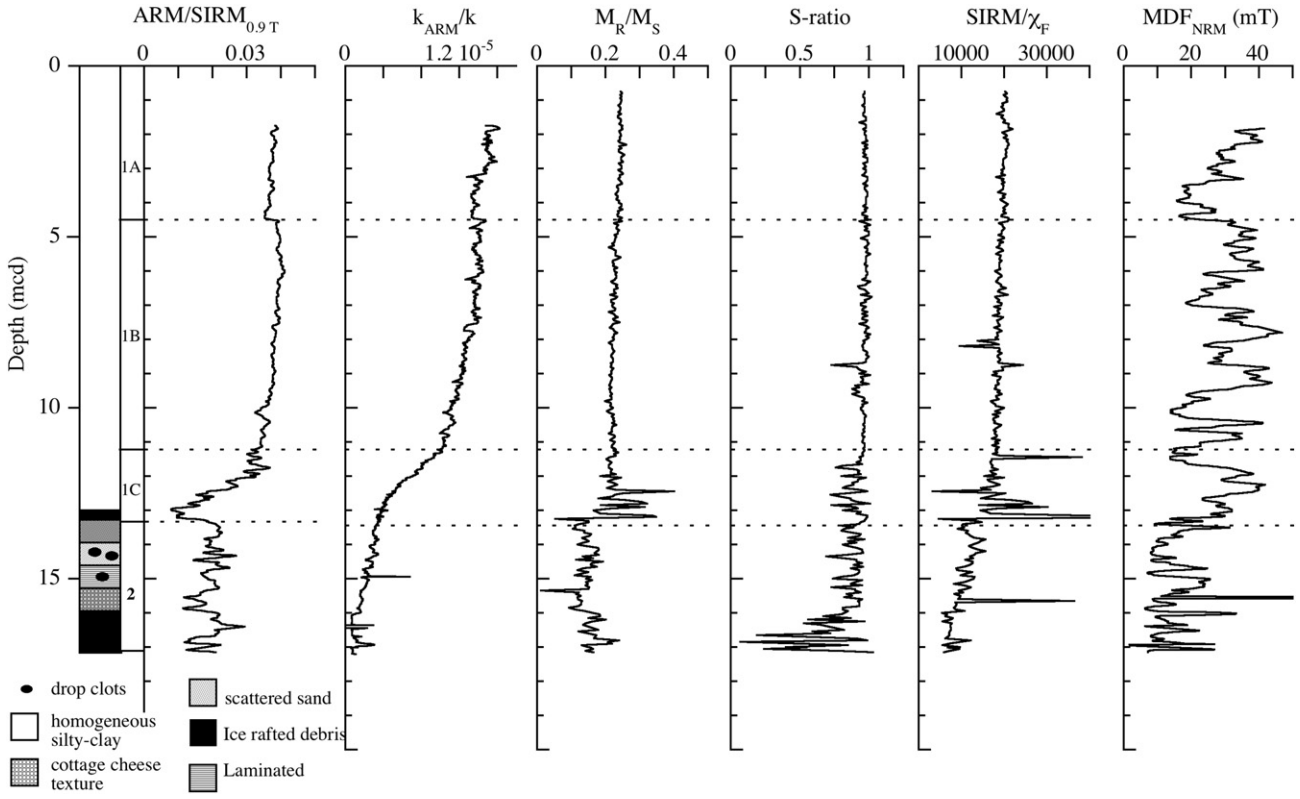

Fig. 6. Lithostratigraphy and magnetic grain-size-dependent and mineralogy-dependent parameters vs. mcd for JPC5. From left to right: ARM normalized by SIRM, susceptibility of ARM (k_{ARM}) normalized by low-field volume-normalized magnetic susceptibility (k), M_R/M_S, MDF_{NRM}, S-ratio, SIRM/χ_F, and MDF_{NRM}. The magnetic particle size and mineralogy is uniform in Unit 1a and 1b, consisting of a mixture of magnetite and iron sulfides. The parameters M_R/M_S, S-ratio, and SIRM/χ_F are unstable in Unit 1c. The MDF_{NRM} shows regularly repeating highs and lows, the only rock magnetic parameter to exhibit this behavior.

titanomagnetite, pyrrhotite, and greigite, which saturate below 300 mT. Samples from this interval saturate between 200 and 300 mT during stepwise IRM acquisition (Fig. 8). From 11.65 mcd to the base of Unit 1, and continuing into Unit 2, S-ratio values oscillate between 0.70 and 1.0, consistent with alternation between a low-coercivity assemblage and high-coercivity minerals such as hematite and goethite (Fig. 6). Within Unit 2 S-ratio values drop to very low values, down to 0.20 and H_{CR} values are high. Darby (unpublished data) examined the mineralogy of individual iron oxide grains in the 45–250 μm fraction using reflected-light microscopy and electron probe microanalysis and observed more abundant ilmenite and hematite grains in Unit 2 than in Unit 1.

The ratio SIRM/χ_F is moderate in Unit 1, varying between 15 and 20 kA/m. These values are consistent with, but not diagnostic of, a mixed assemblage containing magnetite, titanomagnetite, and possibly magnetic iron sulfides (Peters and Thompson, 1998). SIRM/χ_F drops below 5 kA/m in Unit 2 (Fig. 6).

Thermomagnetic curves from Unit 1 show two distinct features in the heating curve, a decrease in susceptibility at 345–370 °C, and a magnetite Curie temperature at 577–586 °C (Fig. 9). The heating and cooling curves are not reversible during cycling to 700 °C, and the 345–370 °C feature is not seen in the cooling curve. Curie temperature runs limited to 0–350 °C cycling are also irreversible, with the cooling curve lower than the heating curve. All samples from Unit 1 show alteration and the growth of magnetic minerals during the experiment, manifested as a sharp increase in susceptibility during heating between 300 and 500 °C, and higher susceptibility values in the cooling curve. The alteration likely results from the breakdown of iron-bearing clay minerals and/or iron sulfides. The 345–370 °C feature becomes muted with depth, and we observed a greater degree of thermochemical alteration in samples from deeper in the core. We do not observe any systematic relationship between S-ratio and Curie temperatures in Units 1a or 1b. Within Unit 1c we observed a reversible Curie temperature at 613 °C in samples with low S ratios. This feature is absent in Unit 1c samples with high S-ratios (Fig. 9).

Low temperature remanence experiments on a magnetic extract from Unit 1a were noisy due to the combination of a very small sample sizes and what we suspect is grain movement inside the sample holder during warming through the oxygen and nitrogen freezing temperatures (60–77 K). However, we do observe a loss of remanence between 90 and 130 K, which spans the temperature range for both the magnetite Verwey transition and the magnetite isotropic point (Dunlop and Özdemir, 1997; Fig. 9). We do not observe the 34 K pyrrhotite transition (Dekkers et al., 1989).

Scanning electron microscope images and energy dispersive X-ray (EDX) spectra of a magnetic extract from 1.0 mcd shows pyrite framboids, iron oxides, and iron-titanium oxides (Fig. 10). We also observed sub-micron, prismatic-shaped and spherical iron sulfide particles (Fig. 10). Each particle is approximately 0.5 μm in length and their EDX spectra contain Fe and S peaks. Each particle is smaller than the interaction volume of the electron beam and neighboring grains contribute to the spectra, which preclude a quantitative chemical analysis. The presence of these particles in a magnetic extract suggests that a ferrimagnetic iron sulfide, either greigite or pyrrhotite, is either the main constituent of the particle, an intergrowth within the particle, or an overgrowth on a non-magnetic substrate such as pyrite (Rowan and Roberts, 2006).

6. Discussion

6.1. Major features of LGM and Holocene Units

The sandy mud and IRD-bearing layers within Unit 2 are undated, but likely represent the deglacial interval through the earliest Holocene (Jakobsson et al., 2005; Polyak et al., 2007; Jakobsson et al.,

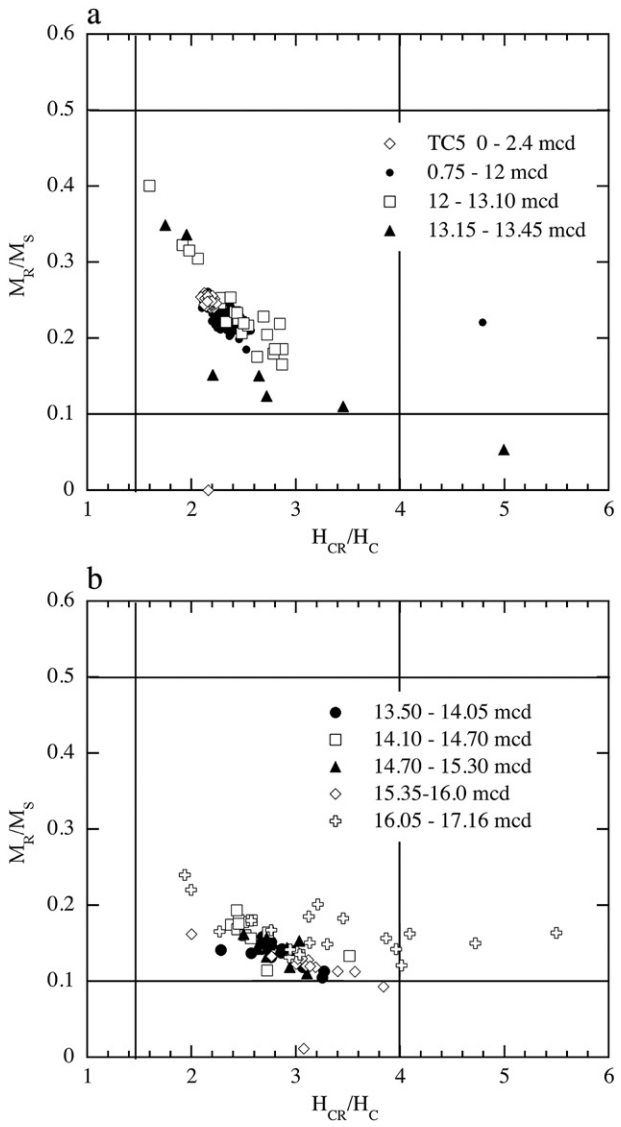

Fig. 7. Magnetic hysteresis parameters for (a) TC5 and JPC5 Unit 1, and (b) JPC5 Unit 2. The Holocene silty-clay has a uniform magnetic particle size. The magnetic mineral assemblage in Unit 2 is coarser and more variable.

2008b). Unit 2 was deposited when JPC5 was receiving coarse sediment from icebergs and sea ice rafting. Ilmenite and titanomagnetite are abundant in the coarse Fe-oxide fraction. Hematite grains and hematite with exsolved ilmenite have slightly elevated counts below approximately 16 mcd, although neither one is abundant in JPC5 (Darby, unpublished data). The presence of ilmenite and hematite are likely responsible for the low S-ratios in Unit 2.

The transition from the deglacial unit to IRD-bearing silty-clay at 13.45 mcd is dated at 9.7 ka (all ages reported are calendar ages BP). The base of Unit 1c is characterized by the presence of detrital carbonate. This IRD-bearing layer is dated at 9.7–9.5 ka. The source of carbonate is the Canadian Arctic including Banks Island, Victoria Island, and the Mackenzie Basin (Bischof and Darby, 2001), which is carried westwards by drifting icebergs. There is no visible carbonate IRD in the core younger than 9.5 ka, nor do we see proxy evidence of IRD layers such as abrupt shifts in magnetic susceptibility or magnetic grain size parameters that would indicate the presence of layers rich in coarse magnetic particles. These observations suggest that ice caps covering the Canadian Arctic islands had retreated onto land by approximately 9.5 ka and could no longer generate icebergs. This is consistent with the results of Hodgson (1994), who date the last ice stream on Victoria Island at 9.6 ka and Dyke et al. (1992) who date the Laurentide terminus to have grounded and ceased calving between 10 and 10.4 ka. In addition, iceberg survivability may have decreased after 9.5 ka possibly as a result of warmer surface waters during the Holocene Thermal Maximum (HTM; Kaufman et al., 2004) in the Arctic. Alternately, iceberg drift patterns may have shifted away from the northwest Alaska margin after 9.5 ka, likely due to the development of the eastward flowing Mackenzie coastal current (McKay et al., 2008, and references therein).

The upper part of Unit 1c from 8.7 to 8.1 ka is characterized by a low concentration of ferrimagnetic material, seen as low values of χ_{LF}, ARM, and SIRM (Fig. 11). Unit 1c is also characterized by total organic carbon (TOC) values that decrease with depth from 11.35 to 13.45 mcd (Lingle et al., 2007; McKay et al., 2008). The low abundance of marine organic carbon likely limits the production of magnetic iron sulfides in this interval (Berner, 1970, 1984).

Magnetic grain size parameters and S-ratio values fluctuate in Unit 1c. S-ratio, H_{CR}, and M_R/M_S values display swings occurring approximately every 180–230 years (Fig. 11). Peaks in M_R/M_S and H_{CR} coincide with high S-ratio values, which suggest periodic input of finer-grained (titano)magnetite to the core site. While thermochemical alteration makes magnetic mineral identification challenging in this interval, we do observe magnetite Curie temperatures throughout this interval and a well-defined, reversible order–disorder temperature at 613–615 °C in samples with low S-ratios (Fig. 10). This Curie temperature is consistent with titanohematite ($Fe_{2-Y}Ti_YO_3$), although we note that homogeneous titanohematite grains are not observed in the coarse Fe-oxide fraction in Unit 2 of JPC5 (Darby, unpublished data), and the "titanohematite" reported in Darby et al. (2009-this volume), is used to describe hematite grains with exsolved ilmenite.

This early Holocene interval of unstable magnetic parameters may be due in part to changes in iceberg and sea-ice source areas or ice-drift patterns controlled by the positions and the strength of the Beaufort Gyre and the Transpolar Drift, which carry different assemblages of coarse Fe-oxides to the Alaska margin (Darby, 2003; Darby and Bischof, 2004). The early Holocene experienced the last remnants of icebergs, and the magnetic fluctuations might be due to a change between icebergs from northern Canada and sea ice from other sources such as Siberia (Darby, 2003; Darby and Bischof, 2004). However, the values of M_R/M_S and S-ratios in this interval, 0.3–0.4 and >0.9, respectively, are indicative of magnetite, specifically fine pseudo single domain to stable single domain grains with diameters of 0.05

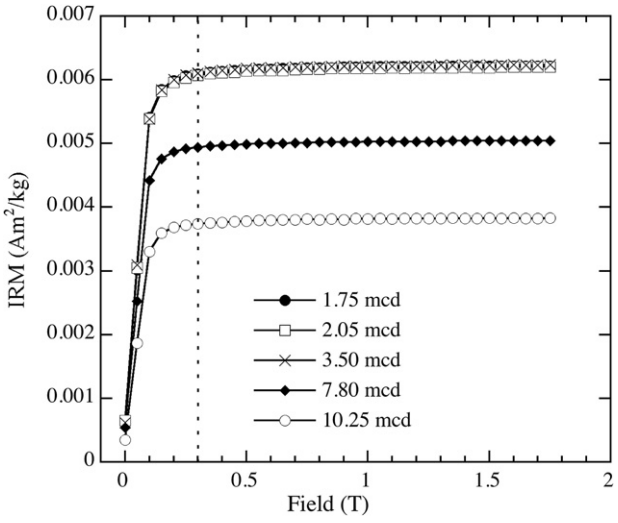

Fig. 8. Step-wise acquisition of isothermal remanent magnetization. Samples from the Holocene silty-clay unit saturate below 300 mT, even those intervals with high values of MDF_{NRM} and low values of S-ratio.

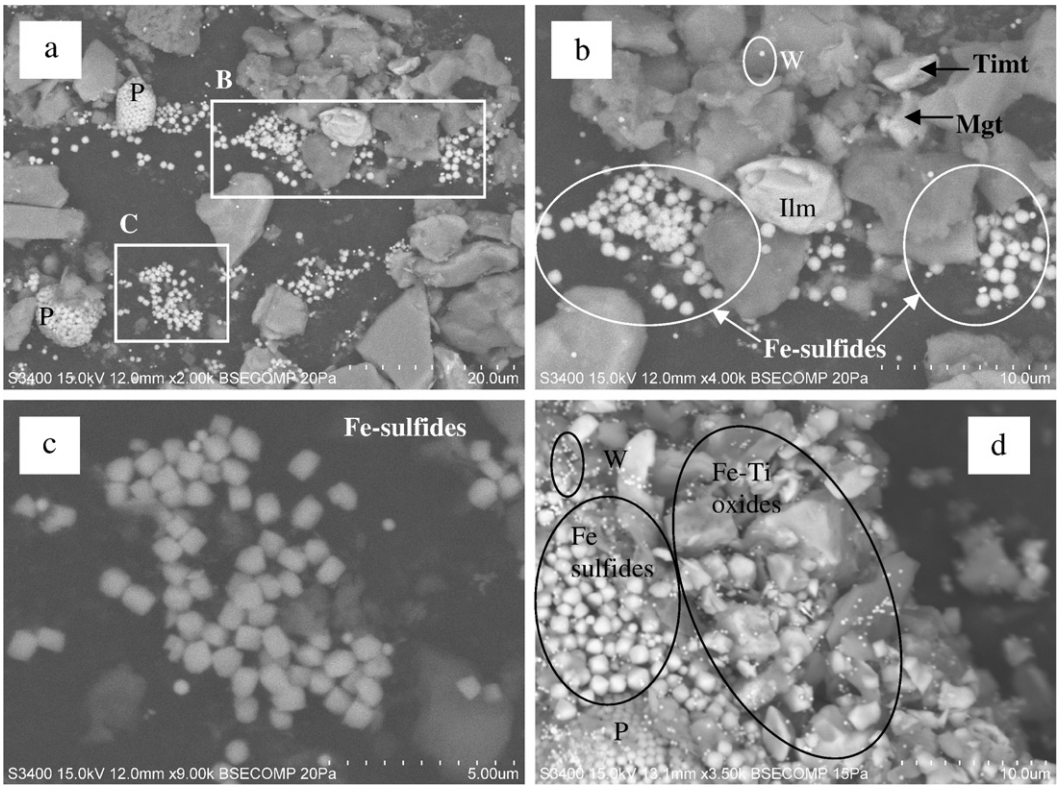

Fig. 9. Scanning electron microscope images of a magnetic extract from JPC5 1.0 mcd. a–d are backscatter electron (BSE) images. The full length of the scale bar is shown at the lower right of each image. Each scale bar is subdivided into 10 equal increments. Mgt = magnetite; Timt = titanomagnetite; Ilm = ilmenite; P = pyrite, W = sodium polytungstate residue from the heavy liquid. a. Overview image of magnetic extract at 2000× magnification showing large iron–titanium oxides and clusters of submicron iron sulfides. Boxed regions show close-up areas in figures b and c. b. Cluster of sub-micron rounded iron sulfide particles. C. Cluster of sub-micron prismatic, iron sulfide particles. d. Cluster of iron–titanium oxides and micron-sized iron sulfides.

to 10 μm (Dunlop and Özdemir, 1997). Grains this small may have been transported by processes other than icebergs and sea-ice rafting, for example river input, sediment transported by currents, or the export of particulate matter from the surface to the seafloor within sinking brines (e.g., Weingartner et al., 1998; Kissel et al., 1999; Sarnthein et al., 2003; Keigwin et al., 2006; Rousse et al., 2006; Darby et al., 2009-this volume).

The timing of this interval partially coincides with the Holocene Thermal Maximum (HTM) in northern Alaska and the Canadian Arctic (Kaufman et al., 2004). The HTM was time transgressive, beginning earlier in the west and later in the east (Kaufman et al., 2004 and references therein). Warmer temperatures during the HTM may have caused glacier recessions and the thawing of permafrost, leading to increased discharge in the rivers that drain into the Arctic Ocean. Fine particles deposited in the Arctic Ocean by rivers may have been carried by currents to the Chukchi–Alaskan margin (Darby et al., 2009-this volume).

Unit 1b spans 8.1 to 3.5 ka, and Unit 1a spans the 3.5 ka to the present. The boundary between Unit 1a and 1b at 3.5 ka is defined by a slightly higher concentration of magnetic material and slightly lower values of ARM/SIRM from 0 to 3.5 ka, indicating coarser magnetic particles from 0 to 3.5 ka (Figs. 6, 11). This boundary is very subtle in JPC5, and the magnetic mineral assemblage appears to be remarkably uniform from 0 to 8.1 ka. Biogenic sedimentation has a negligible effect on the magnetic parameters at this site, as biogenic silica comprises <0.5% of the sediment and biogenic carbonate varies from 0.2 to 0.4% by mass (Lingle et al., 2007; McKay et al., 2008). However, a shift in local conditions at 3.5 ka is consistent with observations from nearby sites, which indicate a period of reduced Pacific water inflow after 3.6 ka (Ortiz et al., 2009-this volume).

6.2. Magnetic iron sulfides in the post-glacial unit

The magnetic mineral assemblage in the post-glacial Holocene unit consists of a mixture of magnetite, titanomagnetite, ilmenite, and magnetic iron sulfides. Black iron sulfides were visually observed throughout the upper 11.15 mcd of JPC5 immediately after the core was split open. All of the concentration-dependent parameters that we measured show the same trend of magnetic mineral concentration gradually decreasing with depth. In addition, the moderately high values of SIRM/χ_F slowly decrease with depth. These observations can be explained by the presence of magnetic iron sulfides throughout Units 1a and 1b, with their abundance gradually decreasing with depth.

The composition of the magnetic iron sulfides is difficult to determine given their low abundance and small particle size, which precludes quantitative identification using scanning electron microscopy. The moderately high values of SIRM/χ_F in the range of 15–20 kA/m (Fig. 6) are more consistent with pyrrhotite than with greigite (Peters and Thompson, 1998). However, the values of SIRM/χ_F >60 kA/m reported for greigite were measured on pure monomineralic samples, whereas JPC5 contains a mixture of several magnetic minerals. Barletta et al., 2008, report extremely stable and well-defined characteristic remanences for JPC5, with maximum angular deviation values <2°. There was no evidence of gyromagnetic remanent magnetization (GRM) acquisition during alternating field demagnetization, which has been reported for greigite-bearing samples (Snowball, 1997a,b; Sagnotti and Winkler, 1999; Hu et al., 2002). However, we observed a decrease in the thermomagnetic hearting curves at 345–370 °C (Fig. 9), which is similar to the high-temperature behavior of greigite reported by Chang et al. (2008). Further, this feature was not reversible in the heating and cooling curves when the experiment

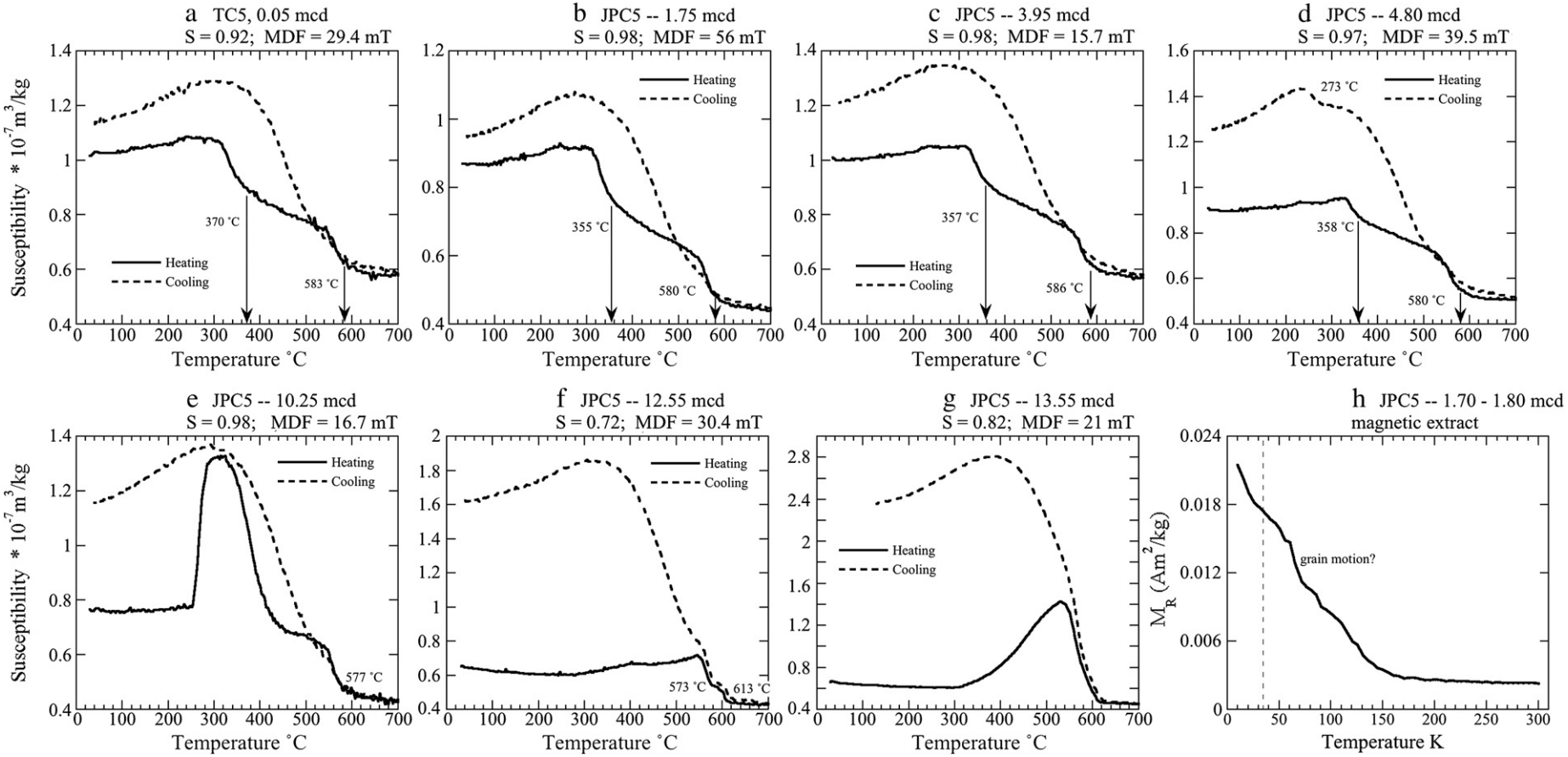

Fig. 10. (a–g) Mass-normalized magnetic susceptibility vs. temperature curves for selected samples. Vertical axes for χ_{LF} plots are in units of 10^{-7} m^3/kg. χ_{LF} features at 340–370 °C and 570–583 °C are attributed to greigite and magnetite, respectively. A Curie temperature at 613 °C in samples with low S-ratios is interpreted as titanohematite. Heating and cooling curves are not reversible, due to the thermochemical alteration of iron-bearing silicates and iron sulfides and production of magnetite during heating. (h) Saturation remanence vs. low temperature for a magnetic extract from 1.70 to 1.80 mcd. M_R was imparted in a 2.5-T field at 10 K and monitored during warming to 300 K. We do not observe the pyrrhotite order/disorder transition at 34 K (dashed line). Loss of M_R between 90 and 130 K is likely due to the combined effects of the magnetite Verwey transition and magnetite isotropic point. We suspect that the loss of M_R at 60–77 K is caused by particles shifting inside the sample holder during warming through the O_2 and N_2 freezing temperatures.

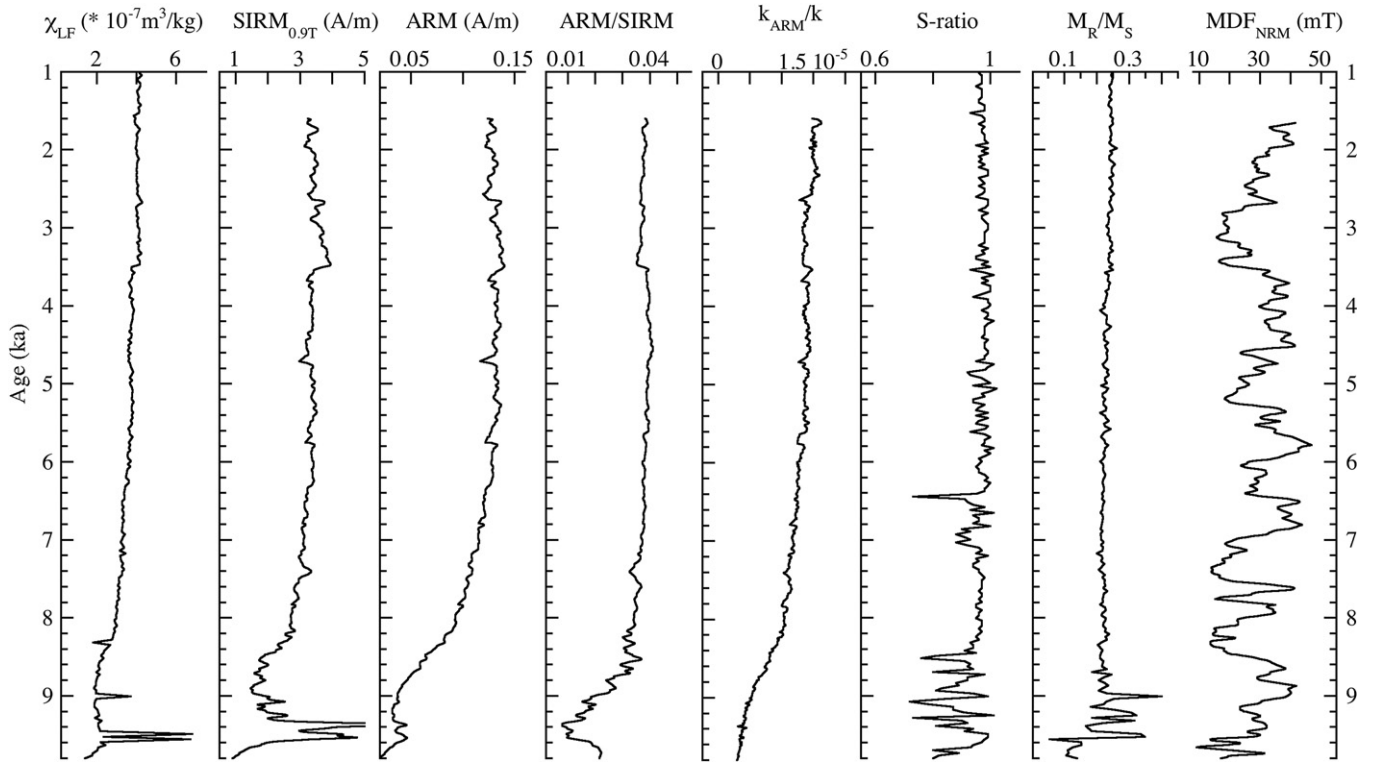

Fig. 11. Magnetic parameters vs. calibrated age for the Holocene interval of JPC5.

was restricted to temperature cycling from 20 to 350 °C, which is also consistent with greigite behavior (e.g., Roberts, 1995; Peters and Dekkers, 2003; Chang et al., 2008). Irreversibility of the 345–370 °C feature argues against this being a titanomagnetite Curie temperature. Hexagonal and monoclinic pyrrhotite have Curie temperatures of approximately 265 °C and 320 °C, respectively, the latter of which is reversible when the experiment is restricted to temperature cycling from 20 to 350 °C (Horng and Roberts, 2006). We did not observe thermomagnetic features in the 265–320 °C temperature range in JPC5. We did not observe the 34 K transition that is associated with pyrrhotite (Dekkers et al., 1989), while greigite has no diagnostic low temperature behavior (Roberts, 1995). In addition, pyrrhotite is unlikely to form during early diagenesis or at temperatures below 180 °C (Horng and Roberts, 2006 and references therein). Therefore, while our observations are not conclusive evidence of greigite, the combination of observations is more plausibly explained by the presence of greigite rather than pyrrhotite.

The magnetite in JPC5 is likely of detrital origin, whereas the magnetic iron sulfides are likely authigenic. Greigite is an intermediate product of pyrite formation during the bacterially-mediated decomposition of organic matter (Berner, 1970, 1984; Canfield and Berner 1987). In the sediment column, the process begins with bacterial reduction of sulfate trapped in interstitial water, which is converted to hydrogen sulfide (H_2S). Sulfate reducing bacteria utilize organic matter as a reductant and energy source. Sulfate will diffuse down the concentration gradient into the sediment, whereas the H_2S will diffuse upwards, where it combines with reactive iron minerals to form iron sulfides. The first sulfide species formed include mackinawite, greigite, and pyrrhotite, which then convert to pyrite of varying morphologies through a variety of pathways that proceed at different rates (e.g., Berner, 1970, 1984; Cutter and Kluckhohn, 1999). The preservation of greigite in sediment indicates that the pyritization process was prevented from running to completion. The pyritization process can be interrupted by a lack of dissolved sulfate, the lack of decomposable organic matter, or lack of reactive iron in detrital minerals (Berner, 1984).

The interplay between the three limiting factors and the magnetic mineral assemblage changes at different levels in JPC5. Unit 1c is characterized by low values of χ_{LF}, ARM, and SIRM, which decrease with depth from 11.15 to 13.45 mcd. k_{ARM}/k and ARM/SIRM are also low and decrease with depth. The magnetic parameters indicate a lower concentration of magnetic material and an overall coarser assemblage, with pulses of fine-grained magnetite supplied every 180–230 years. In Unit 1c the abundance of TOC parallels the magnetic parameters. TOC values are approximately 1.5% at the top of Unit 1c, and decrease steadily down to 13.45 mcd (Lingle et al., 2007; McKay et al., 2008). In this interval the abundance of total sulfur (TS) is very low and nearly zero in some samples (Lingle et al., 2007). TS values rebound at the base of Unit 1b. In Unit 1c we suggest that iron sulfide formation is limited by the lack of decomposable organic carbon. Without this reductant and energy source, sulfate reducing bacteria are unable to produce the H_2S necessary for iron sulfide formation. The lack of magnetic iron sulfides is partly responsible for the low values of χ_{LF}, ARM, and SIRM, combined with the presence of weakly magnetic ilmenite and hematite in the magnetic mineral assemblage.

The relationship between magnetic parameters and iron sulfides is more complex in Units 1a and 1b. Interstitial water samples were not collected from JPC5, therefore we do not know the downcore abundances of dissolved sulfate, H_2S, or Fe. Preliminary TS measurements have been made at a coarse sampling resolution (Lingle et al., 2007), but iron speciation measurements (% of acid volatile sulfides, greigite, and pyrite Cutter and Oatts, 1987) are not yet available. We interpret the consistent values of SIRM/χ_F throughout Units 1a and 1b to mean that greigite is present throughout the Holocene postglacial sediment, although its abundance decreases gradually with depth.

The sedimentation rate at the core site is very high, approximately 145–160 cm/kyr. It is possible that the high sedimentation rate leads to a lack of sulfate in the sediment column. Rapid burial of organic carbon and iron could deplete the available sulfate in the interstitial

water (Berner, 1970, 1984). High deposition rates would require longer diffusion distances and times for sulfate in the bottom water to replenish the sediment porewaters. Without sulfate to reduce there would be insufficient sulfide to convert greigite to pyrite. Low sulfate concentration in the overlying water column could also cause sulfate limitation in the sedimentation. However, we think this scenario is unlikely at the JPC5 core site, where the water depth is 415 m. The base of the low-salinity Pacific layer presently extends to approximately 150 m. The bottom water salinity is presently 34.9‰ (Fig. 2). Freshening the bottom water on the upper continental slope would require significant thickening of the Pacific layer. Such large changes in the Arctic Ocean hydrography would very likely create a sedimentary signature of a low-salinity event across much of the Arctic Ocean, for example in the $\delta^{18}O$ signature of foraminifers. No such signal has been reported (see for example Hillaire-Marcel et al., 2004).

In JPC5 the total organic carbon content (% TOC) is very uniform within Units 1a and 1b, varying between 1.4 and 1.6% and decreasing slightly with depth (Lingle et al., 2007; McKay et al., 2008). The average carbon to nitrogen (C/N) ratio is 6.5–7 at the top of Unit 1a and decreases to 8–10 at the base of Unit 1b (Lingle et al., 2007; McKay et al., 2008). The $\delta^{13}C_{org}$ values also decrease with depth in the core from −23.5‰ at the top of the core to −25.0‰ at the base of Unit 1 (McKay et al., 2008). These observations indicate that the source of organic carbon has changed through time, with more terrestrial organic matter input in the early Holocene, and the proportion of marine organic matter increasing through the Holocene (McKay et al., 2008). Therefore, the reactivity of the organic matter and hence the rate of sulfate reduction has likely changed through time. The addition of marine organic carbon would accelerate sulfate reduction (Berner, 1984), generating more H_2S available for iron sulfide production.

We do not rule out the abundance of reactive iron as a potential limiting factor in the preservation of greigite in JPC5, although we cannot quantify this parameter in this paper. We note that low field magnetic susceptibility values are low in Unit 1, and not substantially higher than high-field (paramagnetic) susceptibility values, indicating a low abundance of ferrimagnetic minerals at this site. Similar to organic carbon, iron mineral reactivity is more important than iron mineral abundance. The half-life for the reaction of iron oxides and iron hydroxides with dissolved sulfide has been investigated by several groups (Canfield, 1989; Canfield et al., 1992; Morse and Wang, 1997). Ferrihydrite and lepidocrocite react quickly with H_2S, with half-lives of hours to several days. Goethite, and hematite have half-lives of approximately 11.5–31 days. Magnetite has a half-life of approximately 105 years, and ilmenite and iron silicates (clays, pyroxene, amphibole, garnet) have half-lives of 230–84,000 years (Canfield et al., 1992). Given the downcore uniformity in the magnetic parameters of JPC5, it is possible that a weakly magnetic phase such as ferrihydrite may impact the iron available for iron–sulfur reactions without significantly affecting the rock magnetic parameters.

6.3. Timing of greigite formation: implications for paleomagnetic and environmental records

The timing of greigite formation has significant implications for the reliability and usefulness of both paleomagnetic data and environmental interpretations based on magnetic parameters (Liu et al., 2004). We suggest that the greigite in JPC5 forms early in the diagenetic process. This interpretation is based on the presence of the greigite identifiers discussed above in sediment as shallow as 5 cm below the sediment-water interface. The upper 15 cm of TC5 contains unsupported ^{210}Pb, and is therefore younger than 100 cal BP. The ^{210}Pb-derived sedimentation rate of 160 cm/kyr in TC5 predicts a depositional age of 30 cal BP at 5 cm depth. Therefore the greigite present at 5 cm must have formed within 30 years of deposition at this site. A 30-year lag between the depositional age of the sediment and the growth of authigenic sulfides is considered negligible for environmental magnetic interpretations, as this is less than the analytical uncertainty of our radiocarbon dates.

6.4. MDF_{NRM} cyclicity

In JPC5 we see very little variability in the rock magnetic parameters in Units 1a and 1b, with the exception of the median destructive field of the natural remanent magnetization (MDF_{NRM}). The MDF_{NRM} displays centennial to millennial-scale fluctuations over the past 9.7 ka, with values ranging from 8 to 55 mT (Fig. 11). The MDF of a remanent magnetization is used to represent the coercivity of the assemblage of remanence-carrying grains. Samples that are resistant to alternating field (AF) demagnetization will have high MDF values, while samples that are easily demagnetized in weak alternating fields will have low MDF values. The MDF_{NRM} is generally higher for stable-single domain (finer) recorders and lower for multidomain (coarser) recorders (Lowrie and Fuller, 1971), although mineralogy, grain shape and particle interactions will also impact the MDF_{NRM} (e.g., Xu and Dunlop 1995; Halgedahl, 1998; Newell 2000). High MDF_{NRM} values could be caused by the acquisition of GRM during AF demagnetization. However, as discussed above, Barletta et al. (2008) report extremely well defined ChRMs with no evidence of GRM acquisition during the demagnetization process. High MDF_{NRM} values could be caused by the presence of high-coercivity minerals such as hematite or goethite, or by the presence of bacterial magnetite. However, we see no evidence of hematite or goethite in the Holocene unit, which has S-ratio values >0.94. Both high and low MDF_{NRM} intervals acquire SIRM in saturating fields below 300 mT. While we have not attempted transmission electron microcopy (TEM) imaging of magnetic extracts to search for bacterial magnetite, we believe this explanation is unlikely due to the probability that fine-grained magnetite particles would dissolve during iron–sulfur diagenesis.

Greigite has higher coercivity than magnetite, yielding high values of M_R, H_C and H_{CR}, and greater resistance to AF demagnetization (higher MDF) in samples containing this mineral (Roberts, 1995). We propose that intervals with high MDF_{NRM} values have more abundant greigite, which formed within 30 years of sediment deposition and contributes to recording the NRM. Intervals with low MDF_{NRM} values have less greigite present, and magnetite is the main mineral contributing to the NRM. We envision three possible scenarios that could create the intervals of low MDF_{NRM} values:

1. Intervals of low MDF_{NRM} reflect times when the rate of sulfidization was slower than the present day, resulting in fewer iron sulfides of any species and particularly less greigite and contributing to the NRM.
2. Intervals of low MDF_{NRM} contain superparamagnetic (SP) particles, which do not contribute to recording the NRM.
3. Intervals of low MDF_{NRM} were times of more complete pyritization, resulting in less greigite and more paramagnetic pyrite in the iron sulfide assemblage.

Total sulfur measurements made at coarse intervals suggest that low MDF_{NRM} intervals coincide with intervals of low TS content, which is consistent with scenario 1. However, it is the speciation between magnetic greigite and non-magnetic AVS and pyrite that is important for our purposes. Until those measurements become available, we attempt to distinguish among the three possibilities using rock magnetic parameters.

We calculated Pearson correlation coefficients between the MDF_{NRM} and other magnetic parameters that are sensitive to magnetic concentration, grain size, and mineralogy (Table 2) according to:

$$\rho_{X,Y} = \frac{Cov(X,Y)}{S_X S_Y} \quad (1)$$

Table 2
MDF_{NRM} correlation coefficients.

Parameter	0–13.15 mcd	0–8.75 mcd	0–6.75 mcd	0–4.5 mcd
Susceptibility	0.02	−0.37	−0.47	−0.34
ARM_O	0.05	−0.31	−0.41	−0.55
$SIRM_O$	−0.04	−0.53	−0.64	−0.62
k_{ARM}/k	0.12	0.23	0.44	0.72
ARM/SIRM	0.11	0.45	0.54	0.62
M_R/M_S	0.07	−0.11	−0.15	0.43
X_F/M_S	0.49	0.06	−0.28	−0.29
X_{HF}	−0.10	0.06	0.33	0.50
H_{CR}	0.09	0.24	0.38	0.54
S-ratio	−0.03	−0.06	−0.08	−0.18
$SIRM/C_F$	−0.01	−0.14	−0.07	0.64
VSF1 Smectite–dolomite	−0.05	−0.03	0.09	0.54
VSF2 Illite–Goethite	−0.14	0.01	0.08	0.49
VSF3–Chlorite	−0.05	−0.22	−0.20	−0.05

where Cov(*X*,*Y*) is the covariance between parameters *X* and *Y*, and *S* is the standard deviation of each data series. The Pearson correlation coefficient ρ varies from −1 to 1, and is zero in the case of independent variables.

Correlation coefficients between MDF_{NRM} and other magnetic parameters are very low, <0.1, when all of Unit 1 is considered. This is due to the decreasing abundance of iron sulfides with depth, controlled by the marine:terrestrial organic carbon composition. The correlation coefficients are slightly higher (absolute values 0.3–0.45) when the comparison is restricted to 0–8.75 mcd, and even higher, (absolute values 0.5–0.64) when the comparison is limited to Unit 1a (0–4.5 mcd). Generally, we observe an inverse relationship between MDF_{NRM} and concentration dependent parameters, i.e., MDF_{NRM} values are low in intervals where χ_{LF}, ARM, and SIRM intensities are high. Low MDF_{NRM} values within intervals of higher concentrations of magnetic material suggest that the amount of reactive iron in the sediment may play a role in driving the pyritization process to completion.

There is no consistent relationship between MDF_{NRM} and grain size dependent parameters. Positive correlation coefficients are observed for MDF_{NRM} and ARM/SIRM and k_{ARM}/k, i.e., MDF_{NRM} values are higher when ARM/SIRM and k_{ARM}/k values are high, which is expected since all of these parameters should respond in the same way to a finer particle size or to the presence of higher coercivity minerals. However, this behavior is limited to Unit 1a. In contrast, the correlation coefficient between MDF_{NRM} and M_R/M_S is negative and <0.1. There is a weak negative correlation between MDF_{NRM} and χ_F/M_S, which tracks SP particles. However, first order reversal curve (FORC) distributions for high MDF_{NRM} and low MDF_{NRM} intervals are identical (not shown). We see no strong evidence for SP particles in low MDF_{NRM} intervals, but note that SP particles are very difficult to observe in bulk sediment unless they are present in high concentrations. There is no systematic correlation between MDF_{NRM} and mineralogy dependent parameters such as $SIRM/\chi_F$ or S-ratio. However, we do observe a correlation coefficient of 0.64 between MDF_{NRM} and $SIRM/\chi_F$ for Unit 1a, which bolsters the connection between elevated MDF_{NRM} and higher concentrations of iron sulfides. There is a weak positive relationship between MDF_{NRM} and X_{HF}, as well as the iron-bearing minerals goethite and smectite as determined by diffuse spectral reflectance measurements (Ortiz et al., 2009-this volume). On the basis of these relationships and previous studies of iron sulfide minerals in marine sediment, we favor option 3, low MDF_{NRM} intervals have experienced a higher degree of pyritization enabled by injections of fresh marine organic matter and possibly injections of reactive iron.

Sagnotti et al. (2001) identified MDF_{NRM} excursions in an Antarctic margin sedimentary record that temporally coincided with northern hemisphere Heinrich events. They argued that the preservation of magnetic iron sulfides in the Antarctic sediment was due to episodes of low phytoplankton productivity and the lack of easily decomposable organic carbon in the sediment column. Intervals of high MDF_{NRM} were carried by magnetite and greigite. Higher phytoplankton productivity and export of organic carbon to the seafloor during interglacials allowed the conversion of greigite to pyrite. During

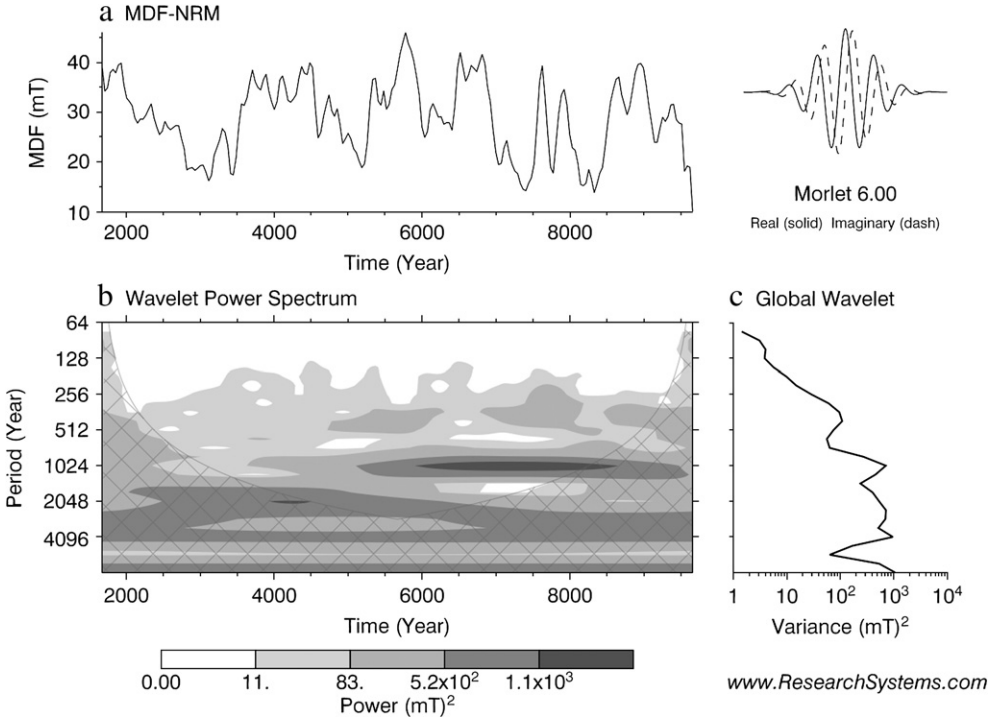

Fig. 12. Wavelet analysis of the MDF_{NRM}. Significant variance is present at periods of 900–1300 years between 8.3 and 6 ka, and a less significant but pervasive signal at periods of 1700–2700 years during the Holocene.

these intervals the MDF_{NRM} was lower and carried solely by magnetite (Sagnotti et al., 2001).

A similar process may be occurring in the Chukchi Sea on shorter timescales. Sea ice coverage and surface water salinity was studied in JPC5 using dinocyst assemblages (McKay et al., 2008). We note that intervals of high MDF_{NRM} coincide with intervals of more extensive sea ice cover, and intervals of low MDF_{NRM} coincide with intervals of less extensive sea ice cover. Times of less extensive sea ice cover would have been times of weaker water column stratification and stronger vertical mixing of the water column (de Vernal et al., 2005). We suggest that during intervals of vertical mixing, recharge of nutrients would have stimulated productivity, increasing the flux of fresh marine organic matter and possibly scavenged reactive iron to the seafloor, allowing a greater degree of pyritization of the iron sulfides. Less greigite would have been preserved, and therefore less greigite would contribute to the recording of the NRM. This interpretation can be tested directly when quantitative measurements of acid volatile sulfide, greigite, and pyrite in JPC5 are made (Cutter and Oatts, 1987; Lingle et al., 2007).

We analyzed the temporal variations in the MDF_{NRM} profile using wavelet analysis, which can identify non-stationary frequencies. We used the Morlet wavelet module available through the online ION program (http://ion.researchsystems.com/cgi-bin/ion-p?page=wavelet.ion). The results indicate significant variance at periods of 900–1300 years present between 8.3 and 6 ka, and a less significant but pervasive variance at periods of 1700–2700 years during the Holocene (Fig. 12). Centennial and millennial cycles have been reported for other high-resolution Arctic and North Atlantic proxy records such as foraminifer abundance, $\delta^{18}O$ profiles, dinocyst assemblages, and IRD abundance. Many of these studies invoke water mass controls and water column stability on the proxy record, such as changes in Atlantic water exported to the Arctic Ocean, sea surface temperature variations, changes in bottom current circulation and discharge, changes in thermohaline circulation, changes in atmospheric pressure fields that affect ice drift (Arctic Oscillation), or tide-driven vertical mixing of the water column (Keeling and Whorf, 2000; Bond et al., 2001; Sarnthein et al., 2003; Andrews and Dunhill, 2004; Darby and Bischof, 2004; de Vernal et al., 2005; Keigwin et al., 2006; Rousse et al., 2006; Hald et al., 2007). Water column stratification in the Chukchi Sea is influenced by the inputs of freshwater from rivers and from lower salinity Pacific waters that enter the Chukchi Sea through the Bering Strait, and the amount of warm, saline Atlantic water entering the Arctic Ocean through the Fram Strait. Less freshwater from these sources would reduce stratification and reduce sea ice formation, and enable greater vertical mixing of the water column. More freshwater from these sources would inhibit vertical mixing. Our record shows periods of high MDF_{NRM} (stronger stratification) at 9.0–8.5 ka, 8.0–7.5 ka, 6.9–6.4 ka cal BP, 6.0–5.3 ka, 4.5–3.5 ka, 3.3 ka, and 2.0–1.6 ka.

7. Conclusions

Core JPC5 from the upper continental slope contains a record of pre-Holocene glacial sedimentation and a high-resolution record of post-glacial Holocene depositional and diagenetic processes. The base of JPC5 consists of 4-m of pre-Holocene glacial sediments that accumulated when the site was influenced by ice proximal conditions or covered by extensive sea ice. The transition to open marine summer conditions occurred at 9.7–9.5 ka, and is marked by the presence of ice rafted debris and peaks in the concentration dependent magnetic parameters. The magnetic mineral assemblage displays abrupt swings in M_R/M_S and S-ratio values between 9.5 and 8.7 ka. High S-ratios and high M_R/M_S values are interpreted as pulses of fine-grained magnetite. This interval overlaps with the time-transgressive Holocene Thermal Maximum, which began earlier in the western Arctic (Kaufman et al., 2004). The fine-grained magnetite could have been supplied by increased river discharge caused by melting glaciers or thawing of permafrost. Alternately, the magnetite could have been carried to the site by currents or sea ice. The magnetic mineral assemblage is very uniform over the last 8.2 ka and consists of a mixture of magnetite and greigite. The amount of greigite is highest at the top of the core and gradually decreases down core. This trend parallels changes in the organic matter composition of JPC5, in which there is a greater proportion of marine organic matter at the top of the core and increasing amounts of terrestrial organic matter downcore (McKay et al., 2008). We propose that the amount of marine organic matter available to power bacterial sulfate reduction controls the degree of pyritization and the amount of greigite preserved in the sediment.

The median destructive field of the NRM (MDF_{NRM}) displays centennial to millennial scale cycles, the only magnetic parameter to exhibit this behavior, with significant variance at periods of 900–1300 and 1700–2700 years. We propose that the MDF_{NRM} is controlled by the variable abundance of greigite formed during early diagenesis. Greigite indicators were observed in modern surface sediment containing unsupported ^{210}Pb and dated as less than 30 years old. We suggest that early-forming greigite contributes to recording the NRM and creates intervals of high MDF_{NRM}. We interpret intervals of high MDF_{NRM} values, which coincide with times of greater sea ice cover (McKay et al., 2008), as times of stronger water column stratification, during which the nutrient supply was limited and phytoplankton productivity levels were reduced. Without organic carbon or reactive iron flux to the seafloor, the pyritization process was interrupted and greigite was preserved. Intervals of low MDF_{NRM} values, which coincide with intervals of less sea ice cover (McKay et al., 2008), are interpreted as times of stronger vertical mixing of the water column, which allowed fresh organic matter and reactive iron to reach the seafloor, driving the pyritization process to completion. The timing of four high MDF_{NRM} intervals, 9.1–8.5 ka, 6–5.3 ka, 4.5–3.5 ka, and 3.3 ka, coincide with globally-observed rapid climate change events associated with polar cooling (Mayewski et al., 2004). Greater water column stratification in the Arctic could be caused by increases in freshwater in the surface layer contributed by river discharge or from Pacific waters entering the Arctic through the Bering Strait.

Acknowledgments

We thank the Captain and crew of the *USCGC* Healy for their extraordinary efforts during cruise HLY05-01. We thank Juliana Pinzon and Luisa Bouhot for laboratory assistance, and Mike Jackson at the Institute for Rock Magnetism for the low-temperature remanence analysis. We thank Leonid Polyak, Greg Cutter, Carie Lingle, and Jennifer McKay for helpful discussions, and Martin Jakobsson and two anonymous reviewers for their constructive comments. This work was funded by NSF grants 0521069, 0612365, and 0619402 to SB, NSF-ARC 0352395 and 0612493 to DD, and NSF-ARC 0520365 and 0612384 to JO. This work also benefited from financial support from NSERC Discovery and Special Research Opportunity (IPY) grants to GSO and from the Polar Climate Stability Network (CFCAS). This is GEOTOP contribution no. 2009–0009.

References

Aagaard, K., Coachman, L.K., Carmack, E., 1981. On the halocline of the Arctic Ocean. Deep Sea Res. A 28, 529–545.
Andrews, J.T., Dunhill, G., 2004. Early to mid-Holocene Atlantic water influx and deglacial meltwater events, Beaufort Sea slope, Arctic Ocean. Quat. Res. 61, 14–21.
Barletta, F., St-Onge, G., Channell, J.E.T., Rochon, A., Polyak, L., Darby, D., 2008. High-resolution paleomagnetic secular variation and relative paleointensity records from the western Canadian Arctic: implication for Holocene stratigraphy and geomagnetic field behaviour. Can. J. Earth Sci. 45, 1265–1281.
Berner, R.A., 1970. Sedimentary pyrite formation. Am. J. Sci. 268, 1–23.
Berner, R.A., 1984. Sedimentary pyrite formation: an update. Geochim. Cosmochim. Acta 48, 605–615.
Bischof, J.F., Darby, D.A., 2001. Mid- to late Pleistocene ice drift in the western Arctic Ocean: Evidence for a different circulation in the past. Science 277, 74–78.

Blanchet, C., Thouveny, N., Vidal, L., Leduc, G., Tachikawa, K., Bard, E., Beaufort, L., 2007. Terrigenous input response to glacial/interglacial climatic variations over southern Baja California: a rock magnetic approach. Quat. Sci. Rev. 26, 3118–3133.
Bond, G., Kromer, B., Beer, J., Muscheler, R., Evans, M.N., Showers, W., Hoffmann, S., Lotti-Bond, R., Hajdas, I., Bonani, G., 2001. Persistent solar influence on North Atlantic climate during the Holocene. Science 294, 2130–2136.
Brachfeld, S., 2006. High-field magnetic susceptibility (χ_{HF}) as a proxy of biogenic sedimentation along the Antarctic Peninsula. Phys. Earth Planet. Inter. 156, 274–282.
Brachfeld, S., Banerjee, S.K., Guyodo, Y., Acton, G.D., 2002. A 13,200 year history of century to millennial scale paleoenvironmental change magnetically recorded in the Palmer Deep, western Antarctic Peninsula. Earth Planet. Sci. Lett. 194, 311–326.
Canfield, D.E., 1989. Reactive iron in marine sediments. Geochim. Cosmochim. Acta 53, 619–632.
Canfield, D.E., Berner, R.A., 1987. Dissolution and pyritization of magnetite in anoxic marine sediments. Geochim. Cosmochim. Acta 51, 645–659.
Canfield, D.E., Raiswell, R., Bottrell, S.H., 1992. The reactivity of sedimentary iron minerals toward sulfide. Am. J. Sci. 292, 659–683.
Chang, L., Roberts, A.P., Tang, Y., Rainford, B.D., Muxworthy, A.R., Chen, Q., 2008. Fundamental magnetic parameters from pure synthetic greigite (Fe_3S_4). J. Geophys. Res. 113B06104. doi:10.1029/2007JB005502.
Codispoti, L.A., Flagg, C., Kelly, V., Swift, J.H., 2005. Hydrographic conditions during the 2002 SBI process experiments. Deep Sea Res. II 52, 3199–3226.
Cutter, G.A., Oatts, T.J., 1987. Determination of dissolved sulfide and sedimentary sulfur speciation using gas chromatography–photoionization detection. Anal. Chem. 59, 717–721.
Cutter, G.A., Kluckhohn, R.S., 1999. The cycling of particulate carbon, nitrogen, sulfur and sulfur species (iron monosulfide, greigite, pyrite, and organic sulfur) in the water columns of Framvaren Fjord and the Black Sea. Mar. Chem. 67, 149–160.
Darby, D.A., 2003. Sources of sediment found in sea ice from the western Arctic Ocean, new insights into processes of entrainment and drift patterns. J. Geophys. Res. 108 (C8), 3257. doi:10.1029/2002JC001350.
Darby, D.A., Bischof, J.F., 2004. A Holocene record of changing Arctic Ocean ice drift analogous to the effects of the Arctic Oscillation. Paleoceanography 19, PA1027.
Darby, D.A., Jakobsson, M., Polyak, L. 2005. Icebreaker expedition collects key Arctic seafloor and ice data. EOS 86(52), 549, 552.
Darby, D.A., Ortiz, J., Polyak, L., Lund, S., Jakobsson, M., Woodgate, R.A., 2009. The role of currents and sea ice in both slowly deposited central Arctic and rapidly deposited Chukchi–Alaskan margin sediments. Global Planet. Change 68, 58–72.
Day, R., Fuller, M., Schmidt, V.A., 1977. Hysteresis properties of titanomagnetites, grainsize and compositional dependence. Phys. Earth Planet. Inter. 13, 260–267.
de Vernal, A., Hillaire-Marcel, C., Darby, D.A., 2005. Variability of sea ice cover in the Chukchi Sea (western Arctic Ocean) during the Holocene. Paleoceanography 20, PA4018. doi:10.1029/2005PA001157.
Dekkers, M.J., Mattei, J.-L., Fillion, G., Rochette, P., 1989. Grain size dependence of the magnetic behavior of pyrrhotite during its low-temperature transition at 34 K. Geophys. Res. Lett. 16, 855–858.
Dunlop, D.J., Özdemir, Ö., 1997. Rock Magnetism: Fundamentals and Frontiers. Cambridge University Press, Cambridge, U.K.
Dyke, A.S., Morris, T.F., Green, D.E.C., England, J., 1992. Quaternary Geology of Prince of Wales Island, Arctic Canada. Mem. – Geol. Surv. Can. 433, 142.
Hagstrum, J.T., Champion, D.E., 2002. A Holocene paleosecular variation record from ^{14}C-dated volcanic rocks in western North America. J. Geophys. Res. 107, 1–14.
Hald, M., Andersson, C., Ebbesen, H., Jansen, E., Klitgaard-Kristensen, D., Risebrobakken, B., Salomonsen, G.R., Sarnthein, M., Sejrup, H.P., Telford, R.J., 2007. Variations in temperature and extent of Atlantic Water in the northern North Atlantic during the Holocene. Quat. Sci. Rev. 26, 3423–3440.
Halgedahl, S.L., 1998. Revisiting the Lowrie–Fuller test: Alternating field demagnetization characteristics of single domain through multidomain glass–ceramic magnetite. Earth Planet. Sci. Lett. 160, 257–271.
Hillaire-Marcel, C., de Vernal, A., Polyak, L., Darby, D., 2004. Size-dependent isotopic composition of planktic foraminifers from Chukchi Sea vs. NW Atlantic sediments — implications for the Holocene paleoceanography of the western Arctic. Quat. Sci. Rev. 23, 245–260.
Hodgson, D.A., 1994. Episodic ice streams and ice shelves during retreat of the northwesternmost sector of the Late Wisconsinan Laurentide Ice Sheet over the central Canadian Arctic archipelago. Boreas 23, 14–28.
Horng, C.-S., Roberts, A.P., 2006. Authigenic or detrital origin of pyrrhotite in sediments?: resolving a paleomagnetic conundrum. Earth Planet. Sci. Lett. 241, 750–762.
Hounslow, M.W., Morton, A.C., 2004. Evaluation of sediment provenance using magnetic mineral inclusions in clastic silicates: comparison with heavy mineral analysis. Sediment. Geol. 171, 13–36.
Hu, S., Stephenson, A., Appel, E., 2002. A study of gyroremanent magnetisation (GRM) and rotational remanent magnetisation (RRM) carried by greigite from lake sediments. Geophys. J. Int. 151, 469–474.
Jakobsson, M., Gardner, J.V., Vogt, P., Mayer, L.A., Armstrong, A., Backman, J., Brennan, R., Calder, B., Hall, J.K., Kraft, B., 2005. Multibeam bathymetric and sediment profiler evidence for ice grounding on the Chukchi Borderland, Arctic Ocean. Quat. Res. 63, 150–160.
Jakobsson, M., Macnab, R., Mayer, M., Anderson, R., Edwards, M., Hatzky, J., Schenke, H.-W., Johnson, P., 2008a. An improved bathymetric portrayal of the Arctic Ocean: implications for ocean modeling and geological, geophysical and oceanographic analyses. Geophys. Res. Lett. 35, L07602. doi:10.1029/2008GL033520.
Jakobsson, M., Polyak, L., Edwards, M., Kleman, J., Boakley, B., 2008b. Glacial geomorphology of the Central Arctic Ocean: the Chukchi Borderland and the Lomonosov Ridge. Earth Surf. Processes Landf. 33, 526–545.
Karlin, R., Levi, S., 1983. Diagenesis of magnetic minerals in recent hemipelagic sediments. Nature 303, 327–330.
Kaufman, D.S., Ager, T.A., Anderson, N.J., Anderson, P.M., Andrews, J.T., Bartlein, P.J., Brubaker, L.B., Coat, L.L., Cwynar, L.C., Duvall, M.L., Dyke, A.S., Edwards, M.E., Eisner, W.R., Gajewski, K., Geirsdóttir, A., Hu, F.S., Jennings, A.E., Mock, C.J., Oswald, W.W., Otto-Bliesner, B.L., Porinchu, D.F., Rühland, K., Smol, J.P., Steig, E.J., Wolfe, B.B., 2004. Holocene thermal maximum in the western Arctic (0–180 °W). Quat. Sci. Rev. 23, 529–560.
Keeling, C.D., Whorf, T.P., 2000. Possible forcing of global temperature by the oceanic tides. Nat. Acad. Sci. 94, 8321–8328.
Keigwin, L.D., Donnelly, J.P., Cook, M.S., Driscoll, N.W., Brigham-Grette, J., 2006. Rapid sea-level rise and Holocene climate in the Chukchi Sea. Geology 34 (10), 861–864. doi:10.1130/G22712.1.
Kissel, C., Laj, C., Lehman, B., Labeyrie, L., Bout-Roumazeilles, V., 1997. Changes in the strength of the Iceland–Scotland overflow water in the last 200,000 years: evidence from magnetic anisotropy analysis of core SU90-33. Earth Planet. Sci. Lett. 152, 25–36.
Kissel, C., Laj, C., Labeyrie, L., Dokken, T., Voelker, A., Blamart, D., 1999. Rapid climatic variations during marine isotopic stage 3: magnetic analysis of sediments from Nordic Seas and North Atlantic. Earth Planet. Sci. Lett. 171, 489–502.
Kissel, C., Laj, C., Clemens, S., Solheid, P., 2003. Magnetic signature of environmental changes in the last 1.2 Myr at ODP Site 1146, South China Sea. Mar. Geol. 201, 119–132.
Korte, M., Genevey, A., Constable, C.G., Frank, U., Schnepp, E., 2005. Continuous geomagnetic field models for the past 7 millennia: 1. A new global data compilation. Geochem. Geophys. Geosyst. 6, 1–28.
Larrasoaña, J.C., Roberts, A.P., Stoner, J.S., Richter, C., Wehausen, R., 2003. A new proxy for bottom-water ventilation in the eastern Mediterranean based on diagenetically controlled magnetic properties of sapropel-bearing sediments. Palaeogeogr. Palaeoclimatol. Palaeoecol. 190, 221–242.
Larrasoaña, J.C., Roberts, A.P., Musgrave, R.J., Gràcia, E., Piñero, E., Vega, M., Martínez-Ruiz, F., 2007. Diagenetic formation of greigite and pyrrhotite in gas hydrate marine sedimentary systems. Earth Planet. Sci. Lett. 261, 350–366.
Leslie, B.W., Lund, S.P., Hammond, D.E., 1990. Rock magnetic evidence for the dissolution and authigenic growth of magnetic minerals within anoxic marine sediments of the California continental borderland. J. Geophys. Res. 95, 4437–4452.
Lingle, C.A., Gipson, B.R., Cutter, G.A., Cutter, L.S., 2007. Biogenic tracers through the Holocene on the Western Arctic Shelf. EOS, Trans. – Am. Geophys. Union 88 (52) Fall Meet. Suppl., Abstract PP51A-0190.
Lisé-Pronovost, A., St-Onge, G., Brachfeld, S., Barletta, F., Darby, D., 2009. Paleomagnetic constraints on the Holocene stratigraphy of the Arctic Alaskan margin. Global Planet. Change 68, 85–99.
Liu, J., Zhu, R., Roberts, A.P., Li, S., Chang, J., 2004. High-resolution analysis of early diagenetic effects on magnetic minerals in post-middle-Holocene continental shelf sediments from the Korea Strait. J. Geophys. Res. B 109 (B03103). doi:10.1029/2003JB002813.
Lowrie, W., Fuller, M., 1971. On the alternating field demagnetization characteristics of multidomain thermoremanent magnetization in magnetite. J. Geophys. Res. 76, 6339–6349.
Mayewski, P.A., Rohling, E.E., Stager, J.C., Karlén, W., Maasch, K.A., Meeker, L.D., Meyerson, E.A., Gasse, F., van Kreveld, S., Holmgren, K., Lee-Thorp, J., Rosqvist, G., Rack, F., Stabuwasser, M., Schneider, R.R., Steig, E.J., 2004. Holocene climate variability. Quat. Res. 62, 243–255.
McKay, J., de Vernal, A., Hillaire-Marcel, C., Not, C., Polyak, L., Darby, D., 2008. Holocene fluctuations in Arctic sea-ice cover: dinocyst-based reconstructions for the eastern Chukchi Sea. Can. J. Earth Sci. 45, 1399–1415.
McNeely, R., Dyke, A.S., Southon, J.R., 2006. Canadian marine reservoir ages, preliminary data assessment. Geol. Survey of Can. Open File Rept., vol. 5049, p. 3.
Morse, J.W., Wang, Q., 1997. Pyrite formation under conditions approximating those in anoxic sediments: II. Influence of precursor iron minerals and organic matter. Mar. Chem. 57, 187–193.
Muhs, D.R., Reynolds, R., Been, J., Skipp, G., 2003. Eolian sand transport pathways in the southwestern United States: importance of the Colorado River and local sources. Quat. Int. 104, 3–18.
Newell, A.J., 2000. The Lowrie–Fuller test: single-domain and micromagnetic theory. Earth Planet. Sci. Lett. 183, 335–346.
Ortiz, J.D., Polyak, L., Grebmeier, J., Darby, D., Eberl, D., Naidu, S., Nof, D., 2009. Provenance of Holocene sediment on the Chukchi-Alaskan margin based on combined diffuse spectral reflectance and quantitative X-Ray Diffraction analysis. Global Planet. Change 68, 73–84.
Peters, C., Dekkers, M.J., 2003. Selected room temperature magnetic parameters as a function of mineralogy, concentration and grain size. Phys. Chem. Earth 28, 659–667.
Peters, C., Thompson, R., 1998. Magnetic identification of selected natural iron oxides and sulfides. J. Magnet. Mag. Min. 183, 365–374.
Polyak, L., Darby, D.A., Bischof, J., Jakobbson, M., 2007. Stratigraphic constraints on late Pleistocene glacial erosion and deglaciation of the Chukchi margin, Arctic Ocean. Quat. Res. 67, 234–245.
Polyak, L., Bischof, J., Ortiz, J.D., Darby, D.A., Channell, J.E.T., Xuan, C., Kaufman, D.S., Løvlie, R., Schneider, D.A., Eberl, D.D., Adler, R., Council, E.A., 2009. Late Quaternary stratigraphy and sedimentation patterns in the western Arctic Ocean. Global Planet. Change 68, 5–17.
Reynolds, R., Reheis, M., Neff, J.C., Goldstein, H., Yount, J., 2006. Late Quaternary eolian dust in surficial deposits of a Colorado Plateau grassland: controls on distribution and ecologic effects. Catena 66, 251–266.
Roberts, A.P., 1995. Magnetic properties of sedimentary greigite (Fe_3S_4). Earth Planet. Sci. Lett. 134, 227–236.

Robinson, S.G., 1986. The late Pleistocene palaeoclimatic record of North Atlantic deep-sea sediments revealed by mineral-magnetic measurements. Phys. Earth Planet. Inter. 42, 22–47.

Rousse, S., Kissel, C., Laj, C., Eiríksson, J., Knudsen, K.-L., 2006. Holocene centennial to millennial-scale climatic variability: evidence from high-resolution magnetic analyses of the last 10 cal kyr off North Iceland (core MD99-2275). Earth Planet. Sci. Lett. 242, 390–405.

Rowan, C.J., Roberts, A.P., 2006. Magnetite dissolution, diachronous greigite formation, and secondary magnetization from pyrite oxidation: unravelling complex magnetizations in Neogene marine sediments from New Zealand. Earth Planet. Sci. Lett. 241, 119–137.

Sagnotti, L., Winkler, A., 1999. Rock magnetism and palaeomagnetism of greigite-bearing mudstones in the Italian peninsula. Earth Planet. Sci. Lett. 165, 67–80.

Sagnotti, L., Macrí, P., Camerlenghi, A., Rebessco, M., 2001. Environmental magnetism of Antarctic Late Pleistocene sediments and interhemispheric correlation of climatic events. Earth Planet. Sci. Lett., 192, 65–80.

Sarnthein, M., Van Kreveld, S., Erlenkeuser, H., Grootes, P.M., Kucera, M., Pflaumann, U., Schulz, M., 2003. Centennial-to-millennial scale periodicities of Holocene climate and sediment injections off the western Barents shelf, 75° N. Boreas 32, 447–461.

Serreze, M.C., Barrett, A.P., Slater, A.G., Woodate, R.A., Aagaard, K., Lammers, R.B., Steele, M., Moritz, R., Meredith, M., Lee, C.M., 2006. The large-scale freshwater cycle of the Arctic. J. Geophys. Res. 111 (C11010). doi:10.1029/2005JC003424.

Snowball, I.F., 1997a. Gyroremanent magnetization (GRM) and the magnetic properties of greigite bearing clays in southern Sweden. Geophys. J. Int. 129, 624–636.

Snowball, I.F., 1997b. The detection of single-domain greigite (Fe_3S_4) using rotational remanent magnetization (RRM) and the effective gyro field (B_g): mineral magnetic and palaeomagnetic applications. Geophys. J. Int. 130, 704–716.

Snowball, I., Torii, M., 1999. Incidence and significance of magnetic iron sulphides in Quaternary sediments and soils. In: Maher, B.A., Thompson, R. (Eds.), Quaternary climates, environments, and magnetism. Cambridge University Press, Cambridge, U.K., pp. 199–231.

Stoner, J.S., Andrews, J.T., 1999. The North Atlantic as a Quaternary magnetic archive. In: Maher, B., Thompson, R. (Eds.), Quaternary Climates, Environments and Magnetism. Cambridge University Press, Cambridge, U.K., pp. 49–80.

Stuiver, M., Reimer, P.J., 1993. Extended C-14 data-base and revised calib 3.0 C-14 age calibration program. Radiocarbon 35, 215–230.

Stuiver, M., Reimer, P.J., Bard, E., Beck, J.W., Burr, G.S., Hughen, K.A., Kromer, B., McCormac, G., Van der Plicht, J., Spurk, M., 1998. INTCAL98 radiocarbon age calibration, 24,000–0 cal BP. Radiocarbon 40, 1041–1083.

Weingartner, T.J., Cavalieri, D.J., Aagaard, K., Sasaki, Y., 1998. Circulation, dense water formation, and outflow on the northeast Chukchi shelf. J. Geophys. Res. 103 (C4), 7647–7661.

Woodgate, R.A., Aagaard, K., Swift, J.H., Falkner, K.K., Smethie Jr., W.M., 2005. Pacific ventilation of the Arctic Ocean's lower halocline by upwelling and diapycnal mixing over the continental margin. Geophys. Res. Lett. 32 (L18609). doi:10.1029/2005GL023999.

Xu, S., Dunlop, D.J., 1995. Toward a better understanding of the Lowrie–Fuller test. J. Geophys. Res. 100, 22533–22542.